HHS Public Access

Author manuscript

J Neurochem. Author manuscript; available in PMC 2024 October 01.

Published in final edited form as:

J Neurochem. 2023 October ; 167(1): 16–37. doi:10.1111/jnc.15880.

Clustering of $Ca_V1.3$ L-type calcium channels by Shank3

Qian Yang[1], **Tyler L. Perfitt**[1,5], **Juliana Quay**[2], **Lan Hu**[1], **Dorian Lawson-Qureshi**[1], **Roger J. Colbran**[1,3,4]

[1]Department of Molecular Physiology and Biophysics, Vanderbilt University School of Medicine, Nashville, TN, USA 37232-0615

[2]Chemical and Physical Biology, Vanderbilt University School of Medicine, Nashville, TN, USA 37232-0615

[3]Vanderbilt Brain Institute, Vanderbilt University School of Medicine, Nashville, TN, USA 37232-0615

[4]Vanderbilt-Kennedy Center for Research on Human Development, Vanderbilt University School of Medicine, Nashville, TN, USA 37232-0615

[5]Current address: Rare Disease Research Unit, Pfizer Inc

Abstract

Clustering of L-type voltage-gated Ca^{2+} channels (LTCCs) in the plasma membrane is increasingly implicated in creating highly localized Ca^{2+} signaling nanodomains. For example, neuronal LTCC activation can increase phosphorylation of the nuclear CREB transcription factor by increasing Ca^{2+} concentrations within a nanodomain close to the channel, without requiring bulk Ca^{2+} increases in the cytosol or nucleus. However, the molecular basis for LTCC clustering is poorly understood. The postsynaptic scaffolding protein Shank3 specifically associates with one of the major neuronal LTCCs, the $Ca_V1.3$ calcium channel, and is required for optimal LTCC-dependent excitation-transcription coupling. Here, we co-expressed $Ca_V1.3$ α1 subunits with two distinct epitope-tags with or without Shank3 in HEK cells. Co-immunoprecipitation studies using the cell lysates revealed that Shank3 can assemble complexes containing multiple $Ca_V1.3$ α1 subunits under basal conditions. Moreover, $Ca_V1.3$ LTCC complex formation was facilitated by $Ca_V\beta$ subunits (β3 and β2a), which also interact with Shank3. Shank3 interactions with $Ca_V1.3$ LTCCs and multimeric $Ca_V1.3$ LTCC complex assembly were disrupted following the addition of Ca^{2+} to cell lysates, perhaps simulating conditions within an activated $Ca_V1.3$ LTCC nanodomain. In intact HEK293T cells, co-expression of Shank3 enhanced the intensity of membrane-localized $Ca_V1.3$ LTCC clusters under basal conditions, but not after Ca^{2+} channel activation. Live cell imaging studies also revealed that Ca^{2+} influx through LTCCs disassociated Shank3 from $Ca_V1.3$ LTCCs clusters and reduced the $Ca_V1.3$ cluster intensity. Deletion of the Shank3 PDZ domain

Address correspondence to: Roger J. Colbran, Rm. 702 Light Hall, Vanderbilt University School of Medicine, Nashville, TN 37232-0615 (Tel: 615-936-1630. Fax: 615-322-7236. roger.colbran@vanderbilt.edu).

Author contributions

Q.Y. and R.J.C designed research; Q.Y., T.L.P. and D.L performed biochemistry experiments; Q.Y. performed imaging experiments; L.H. prepared rat hippocampal neuronal cultures; Q.Y. and J.Q. analyzed data; Q.Y. and R.J.C. wrote the manuscript; J.Q. helped to modify the manuscript. All authors participated in the discussion, revision, and approval of the final manuscript.

Conflict of interest disclosure

The authors declare that they have no competing interests.

prevented both binding to $Ca_V1.3$ and the changes in multimeric $Ca_V1.3$ LTCC complex assembly *in vitro* and in HEK293 cells. Finally, we found that shRNA knock-down of Shank3 expression in cultured rat primary hippocampal neurons reduced the intensity of surface-localized $Ca_V1.3$ LTCC clusters in dendrites. Taken together, our findings reveal a novel molecular mechanism contributing to neuronal LTCC clustering under basal conditions.

Graphical Abstract

Clustering of L-type voltage-gated Ca^{2+} channels (LTCCs) in the plasma membrane is increasingly implicated in creating highly localized Ca^{2+} signaling nanodomains. Left panel: Our data support the clustering of multiple $Ca_V1.3_L$ L-type calcium channels by the neuronal scaffolding protein Shank3 via direct interaction of the Shank3 PDZ domain with the C-terminal domain of $Ca_V1.3_L$ under basal conditions. Right panel: Ca^{2+} influx via $Ca_V1.3_L$ causes disassociation of Shank3 from $Ca_V1.3_L$, disrupting Shank3-mediated clustering of $Ca_V1.3_L$ channels. Shank3-mediated $Ca_V1.3_L$ clustering under basal conditions may have a key role in downstream signaling, such as excitation-transcription coupling and neuronal plasticity.

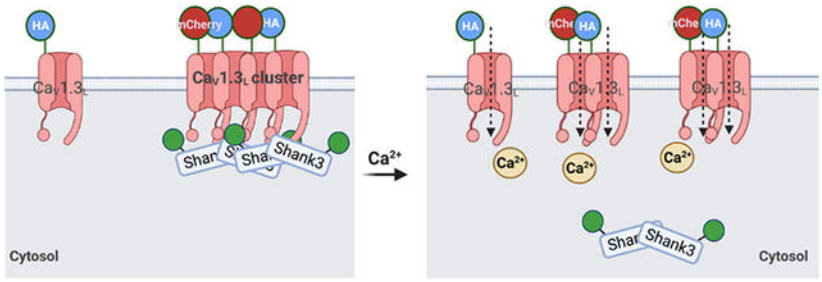

Introduction

Voltage-gated L-type calcium channels (LTCCs) are widely expressed in the central nervous system, endocrine cells, atrial myocytes, and cardiac pacemaker cells, and regulate numerous physiological processes (Catterall, 2011; Striessnig & Koschak, 2008). Clustering of the major neuronal LTCC subtypes, $Ca_V1.2$ and $Ca_V1.3$, amplifies Ca^{2+} influx in local Ca^{2+} nanodomains (Dixon et al., 2012; Moreno et al., 2016; Navedo & Santana, 2013) that can be sufficient to initiate some downstream pathways, without requiring Ca^{2+} increases in the bulk cytosol or nucleus (Deisseroth et al., 1996; Stern, 1992; Tadross et al., 2013). The potential importance of LTCC clustering in creating these Ca^{2+} nanodomains has been recognized, but the molecular basis for cluster formation is incompletely understood.

LTCCs are comprised of a pore-forming α1 subunit that co-assembles with auxiliary $Ca_V\beta$, $Ca_V\alpha2\delta$ and $Ca_V\gamma$ subunits (Simms & Zamponi, 2014). The C-terminal domains of $Ca_V1.2$ and $Ca_V1.3$ α1 subunits play an important role in modulating LTCC cell surface expression and downstream signaling. For example, deletion of the C-terminal PDZ domain-interacting motif from $Ca_V1.2$ or $Ca_V1.3$ interferes with excitation-transcription (E-T) coupling (Weick et al., 2003; Zhang et al., 2005). Alternative mRNA splicing gives rise to long and short forms of the $Ca_V1.3$ α1 subunit C terminal domain ($Ca_V1.3_{42}$ or $Ca_V1.3_L$; $Ca_V1.3_{42A}$ or $Ca_V1.3_S$; $Ca_V1.3_{43S}$), which alters voltage- and Ca^{2+}-dependent gating properties (Bock

et al., 2011; Hui et al., 1991; Moreno et al., 2016; Singh et al., 2008; Tan et al., 2011). Scaffolding proteins containing PDZ domains, such as Shank3, densin, and erbin interact with the C-terminal PDZ domain-interacting motif of $Ca_V1.3_L$, but not $Ca_V1.2$ or $Ca_V1.3_S$, to differentially modulate the levels and pattern of cell surface $Ca_V1.3_L$ expression and/or $Ca_V1.3_L$ activity (Calin-Jageman et al., 2007; Jenkins et al., 2010; Stanika et al., 2016; Zhang et al., 2005). However, both $Ca_V1.3_L$ and $Ca_V1.3_S$ were reported to form similar clusters in the plasma membrane that were estimated to contain an average of 8 α1 subunits in neurons (Moreno et al., 2016). Interestingly, calmodulin (CaM) binds to preIQ and IQ motifs in the C-terminal domain to facilitate cooperative channel opening of $Ca_V1.3_S$, but not $Ca_V1.3_L$, and Ca^{2+} influx (Moreno et al., 2016). Collectively these findings suggest an important role for the α1 subunit C-terminal domain in regulating LTCC activity and surface expression, as well as E-T coupling.

Of the PDZ-domain containing proteins that bind to the C-terminal domain of $Ca_V1.3_L$, Shank3 has been most intensively studied, in part because it is a multi-domain postsynaptic scaffolding protein strongly linked to multiple neuropsychiatric disorders. Previous studies found that Shank3 facilitates synaptic $Ca_V1.3_L$ surface expression (Zhang et al., 2006; Zhang et al., 2005). However, Shank has no substantial effect on the biophysical properties of $Ca_V1.3$ channels when co-expressed in Xenopus oocyte (Zhang et al., 2005). In addition, Shank3 is required for normal downstream LTCC signaling to the nucleus (Perfitt et al., 2020; Pym et al., 2017; Zhang et al., 2006; Zhang et al., 2005). Although the C-terminal SAM domains of Shank3 have been shown to mediate “tail-to-tail” multimerization (Sheng & Kim, 2000), potentially facilitating the assembly of larger multi-protein complexes, the role of Shank3 in $Ca_V1.3$ LTCCs clustering is poorly understood.

Here, we show that Shank3 facilitates the assembly of complexes containing multiple $Ca_V1.3_L$ α1 subunits *in vitro* and on the surface of intact HEK293 cells, and that clustering is further enhanced by Ca_Vβ subunits. This robust Shank3-dependent clustering under basal conditions is disrupted by the addition of Ca^{2+} *in vitro*, or by LTCC activation in HEK cells. Moreover, we found that knock-down of Shank3 expression disrupted basal cell surface $Ca_V1.3_L$ clustering in the dendrites of cultured rat hippocampal neurons. Taken together, our data indicate that Shank3 assembles $Ca_V1.3_L$ LTCCs clusters under basal conditions, which may be important for downstream Ca^{2+} signaling.

Experimental procedures

DNA constructs

Original sources of DNA constructs are provided in the Key Resources Table. The Shank3 construct containing a deletion of the PDZ domain (GFP-Shank3-ΔPDZ) was generated by in-frame PCR deletion of the entire 270 bp region encoding ^{572}Iso-Val^{661} from the parent GFP-Shank3 construct. Sequences of all constructs were confirmed by DNA sequencing. The home-made constructs can be shared upon reasonable request.

The addition of an HA-tag to the $Ca_V1.2$ or $Ca_V1.3$ cytosolic N-terminal domain or to the extracellular S5-H5 loop of domain II has minimal if any effects on channel properties (sHA-$Ca_V1.3$: (Jenkins et al., 2010); (Gregory et al., 2011); sHA-$Ca_V1.2$: (Altier et al.,

2002); HA-$Ca_V1.3$: (Zhang et al., 2005)); these constructs have been used previously for immunocytochemistry (Gregory et al., 2011; Jenkins et al., 2010; Obermair et al., 2010; Stanika et al., 2016; S. Wang et al., 2017) and co-immunoprecipitation (Abiria & Colbran, 2010; X. Wang et al., 2017). Addition of a GFP tag to the N-terminal domain of $Ca_V1.2$ or $Ca_V1.3$ also has little effect on channel properties (Costé de Bagneaux et al., 2018; Obermair et al., 2010; Obermair et al., 2004; Vierra et al., 2019). The mCherry-tagged $Ca_V1.3$ channel was created from the GFP-$Ca_V1.3$ construct by replacing GFP with mCherry, which is similar in size.

Culture and transfection of HEK cells

Authenticated HEK293 and HEK293T cells were purchased from ATCC (see Key Resources Table). HEK293 cells, but not HEK293T cells, are included on a list of commonly misidentified cell lines (https://iclac.org/databases/cross-contaminations/, version 12); however, no further cell line authentication was performed. Cells were grown at 37°C and 5% CO_2 in DMEM plus 10% (v/v) fetal bovine serum (Gibco), 1% (w/v) penicillin/streptomycin (Gibco), 1% (v/v) MEM non-essential amino acid solution (Sigma, catalog no. RNBK3078), and 1% GlutaMAX (Gibco, catalog no. 2248970), and passaged a maximum of 20 times before transfection. Cells were co-transfected at ~70% confluence using Lipofectamine 2000 (Invitrogen). HA-$Ca_V1.3_L$ and α2δ with or without mCherry-$Ca_V1.3_L$ were co-expressed with empty Flag vector or vectors encoding FLAG-β3 or -β2a together with vectors encoding GFP or GFP-Shank3 (WT or with PDZ deletion), as indicated (ratio of α1: α2δ: β: Shank3 was 3:1:1:1.5). For co-immunoprecipitation and GST pulldown experiments, HEK293T cells were transfected using a total of ≤10 μg of DNA per 10-cm culture dish (Corning, catalog no. 430167). The medium was completely changed 24 h after transfection and cells were harvested after 48 h for co-immunoprecipitation or GST pulldown assay. For immunostaining and live-cell imaging, HEK293 cells, which generally express lower levels of recombinant proteins, were transfected with ≤2 μg of DNA per well of a 6-well plate. Cells were re-plated at low density 24 h after transfection into a 24-well plate with 12×12 mm^2 coverslips (Fisher Scientific, catalog no. 22293232) or into a 29 mm dish with 10 mm bottom well (Cellvis, catalog no. D29-10-1.5-N) for live-cell imaging. Cells were grown for another 24-48 h before treatment and fixation, or live-cell imaging.

Co-immunoprecipitation (Co-IP)

Transfected cells were lysed in lysis buffer (50 mM Tris-HCl pH 7.5, 150 mM NaCl, 1 mM EDTA, 1 mM EGTA, 1 mM DTT, 1% Nonidet P-40 (v/v), 1 mM Microcystin-LR, and protease inhibitor mixtures). Cell lysates were homogenized (15-25 bursts; Duty Cycle %: 30; Output Control level: 2, 80 watts) with Branson Sonifier 450 (VWR SCIENTIFIC) and then were cleared by low-speed centrifugation (500 x g). The supernatant was then incubated at 4°C for 4 h with rabbit anti-HA (1 μg in 500 μl cell lysate; Figures 2A, 4B and 5A) or 1 h with rabbit anti-GFP (0.5 μg in 500 μl cell lysate; Figure 3A) or for 2-3 h with mouse anti-Flag M2 antibody (1 μg in 500 μl cell lysate; Figure 3C) and 10 μl of prewashed Dynabeads Protein A (Thermo Fisher Scientific, catalog no. 10002D; for rabbit antibodies) or Dynabeads Protein G (Thermo Fisher Scientific, catalog no. 10004D; for mouse antibodies). Where indicated, lysates were supplemented with 2 mM $CaCl_2$ and/or 1 μM calmodulin with or without 50 μM

calmidazolium (final concentrations) prior to incubation; the free Ca^{2+} concentration was ~200 μM, calculated using MaxChelator (https://somapp.ucdmc.ucdavis.edu/pharmacology/bers/maxchelator/webmaxc/webmaxcS.htm). Beads were isolated magnetically and washed three times using lysis buffer (supplemented with 2 mM $CaCl_2$ for the relevant samples) before eluting proteins using 2X SDS-PAGE sample buffer.

GST pulldown

GST-Shank3 constructs were created, expressed, and purified as previously described (Perfitt et al., 2020). Transfected cell supernatants (see above) were incubated at 4°C with ~150 nM of the indicated full-length GST fusion proteins (or GST control) and 10 μl prewashed glutathione magnetic beads for 1-2 h. Beads were then separated magnetically and washed three times with GST pulldown buffer (50 mM Tris-HCl pH 7.5; 200 mM NaCl; 1% (v/v) Triton X-100). GST protein complexes were eluted by incubation with 40 μl of 20 mM glutathione (pH 8.0) (Sigma) in GST pulldown buffer at 4°C for 10 min.

CaMKII Autophosphorylation

Mouse CaMKIIα was expressed and purified essentially as described previously (McNeill & Colbran, 1995) and bovine brain calmodulin was expressed and purified essentially as described (Bartlett et al., 2003; Gopalakrishna & Anderson, 1982). CaMKIIα (0.25 μM) was incubated at 30°C with 50 mM HEPES, pH 7.5, 10 mM Mg(Ac)2, 0.5 mM CaCl2, 1 or 5 μM calmodulin, 0.5 mM ATP for 20 s in the absence or presence of 50 μM calmidazolium (TOCRIS). Samples were stopped by adding 4X SDS-PAGE sample buffer, then heated at 65°C for 5 min, and resolved on an SDS-PAGE gel for Western blotting. Purified CaMKIIα and calmodulin can be shared upon reasonable request.

Western blot analysis

Samples were resolved on 10% (Figures 1, 2, and 3A; Figure S1) or 7.5% (Figures 3C, 4 and 5) SDS-PAGE gels and transferred to nitrocellulose membrane (Protran, Camp Hill, PA). Membranes were blocked in blotting buffer containing 5% nonfat dry milk, 0.1% (v/v) Tween-20, in Tris-buffered saline (20 mM Tris, 136 mM NaCl), pH 7.4 for 1 h at room temperature. The membrane was incubated at 4°C with primary antibody (rabbit anti-HA, mouse anti-CaMKII, and donkey anti-rabbit 680LT were diluted 1:8000; all the other antibodies were diluted 1:4000) in blotting buffer overnight. After washing with washing buffer (0.1% (v/v) Tween 20 in Tris-buffered saline) two times (10 min/time), membranes were incubated with IR dye-conjugated (all replicates of GST-pulldown experiments and most replicates of Co-IP experiments) or HRP-conjugated secondary antibody (three replicates of the Co-IP experiments in Figure 5) for 1 h at room temperature and washed again before development. Infra-red images of blots were collected using an Odyssey system (LI-COR Biosciences). Blots incubated with HRP-conjugated secondary antibodies were incubated with the Western Lightening Plus-ECL, enhanced chemiluminescent substrate (PerkinElmer, Waltham, MA) and visualized using Premium X-ray Film (Phenix Research Products, Candler, NC) exposed in the linear response range. Images were quantified using Fiji software (RRID: SCR_003070). Background signals in equivalent areas from the negative control lanes were subtracted from signals in the experimental lanes. Similar

results were obtained when the same samples were analyzed in parallel using ECL and Odyssey-based methods in some studies.

HEK cell stimulation

BayK 8644 (BayK) was prepared as a 50 mM stock solution in DMSO. For the experiment in Figure 8, transfected HEK293 cells (see above) were incubated in HEPES buffer (150 mM NaCl, 5 mM KCl, 2 mM $MgCl_2$, 10 mM HEPES pH 7.4, 10 mM Glucose) for 10 min. Cells from different wells were then switched to each of these conditions: HEPES buffer + DMSO (0.02% v/v), HEPES buffer + BayK (10 μM), 2.5 mM Ca^{2+} buffer (HEPES buffer + 2.5 mM $CaCl_2$) + DMSO, or 2.5 mM Ca^{2+} buffer + BayK for 10-15 min each. After a further 10-15 min, cells were fixed using ice-cold 4% paraformaldehyde containing 4% sucrose in 0.1 M Phosphate Buffer (pH 7.4) for 10 min. Cells expressing mCherry-$Ca_V1.3$ and GFP or GFP-Shank3 (WT or ΔPDZ) (Figure 8) were washed three times with PBS after fixation, mounted on slides using Prolong Gold Antifade Mountant, and then stored at 4°C for imaging.

Total Internal Reflection Fluorescence (TIRF) Microscopy

All HEK cell imaging was performed using a Nikon Multi Excitation TIRF microscope with a 60x/1.49 n.a. TIRF objective (Nikon, Tokyo, Japan), Andor Xyla sCMOS camera (Andor, Belfast, UK); 405-, 488-, 561-, and 640 nm solid-state lasers (Nikon LU-N4); HS-625 high-speed emission filter wheel (Finger Lakes Instrumentation, Lima, NY); and standard filter sets. Images were acquired using NIS-Elements (Nikon) with the same exposure time of 30-100 ms for both channels and 3-5% laser power for 488 nm and 10-15% laser power of 561 nm. Identical imaging parameters were used for all cover slips within the same biological replicate.

For the long-term time-lapse imaging of live HEK293 cells, the live tissue chamber (TOKAI HIT, Japan) with atmosphere heater, stage heater, humidity, and CO_2 control was used. Perfect Focus (PFS) was on during the whole imaging session to hold the correct focal plane. The imaging interval was set as 5 seconds, and the duration of each treatment phase was 2-3 minutes (Figure 7) or 5-10 min (Figure 6). In Figures 7, cells were first imaged in 0 Ca^{2+} HEPES buffer (see above). Image collection was paused and the buffer was changed to HEPES buffer + 10 μM BayK for the 2nd imaging phase and then to 2.5 mM Ca^{2+} buffer + 10 μM BayK for the 3rd imaging phase. The time gap between each phase was about one minute. The position of target cells was confirmed after each buffer change before resuming image collection.

All images were opened and processed in Fiji software. The GFP channel and the Polygon Selection tool were used to select the region of interest (ROI) corresponding to the outline of each cell. The background was flattened and the mCherry-$Ca_V1.3$ ROIs were thresholded based on the fluorescence signal. The threshold was defined using the mean intensity of mCherry plus two-times the standard deviation. Analyze Particles was used to calculate the intensity, area, and number of mCherry-$Ca_V1.3$ clusters above the threshold in each ROI. Cluster density was calculated using the cluster number divided by ROI area. For mCherry-$Ca_V1.3$ intensity analysis in images of live cells, ROIs that include at least four mCherry

clusters colocalized with GFP-Shank3 were used for quantification, and Analyze Particles was applied to all-time series. For colocalization analysis, GFP and mCherry channels were automatically thresholded before calculating the intensity correlation quotient (ICQ), which quantifies co-localization from complete segregation to perfect overlap on a −0.5 to +0.5 scale, as previously described (Li et al., 2004; Perfitt et al., 2020).

Tracking of mCherry-Ca_V1.3 LTCC clusters on the cell surface

The motility of mCherry-tagged Ca_V1.3 clusters with or without Shank3 co-expression was compared by automatic tracking using TrackMate in Fiji. LoG detector was used, and the estimated diameter of particles was set to 0.8 μm. Then, HyperStack Displayer was selected as the viewer mode. Quality was added as a filter to rule out the background selection and spots color was set by mean intensity. Finally, Simple LAP Tracker was used, and the maximum frame gap was set to 2 (one or two missing time points were allowed while tracking). The linking and gap-closing maximum distance was adjusted individually depending on the observation of satisfactory trajectories from frame to frame by visual inspection to avoid false connections. The dynamic parameter (including track ID, displacement, duration, X, Y, Z location, and mean speed of the event being tracked) of all tracks were exported from Fiji for further analysis.

Primary hippocampal neuron cultures and immunocytochemistry

Dissociated hippocampal neurons were prepared from E18 Sprague Dawley rat embryos, as previously described (Shanks et al., 2010). A total of 36 embryos from 6 dams were used to generate primary cultures for these studies. Embryonic brains were dissected and pooled to prepare the cultures, so presumably, the cultures contain an ~50:50 mix of neurons from male and female embryos. Neurons were transfected at 14 days *in vitro* (DIV) using Lipofectamine 2000 following the manufacturer's directions (Thermo Fisher Scientific). sHA-Ca_V1.3/sHA-Ca_V1.2, α2δ, and FLAG-β subunit (β3 or β2a) were co-transfected with GFP-nonsense shRNA (nssh) or GFP-Shank3-shRNA or GFP-Shank3 (ratio of α1: α2δ: β: GFP was 3:1:1:1). A total of 1 μg of DNA was transfected for each well of a 12-well plate; after 2-3 hours neurons were switched back to the conditioned medium. Neurons were used for immunostaining at DIV20-21. All procedures were pre-approved by the Vanderbilt University Institutional Animal Care and Use Committee (protocol number: M1600253) and followed the National Institutes of Health Guide for the Care and Use of Laboratory Animals.

Neurons were live-stained for surface sHA-Ca_V1.3 labeling. Briefly, half of the conditioned medium (500 μl) was collected for secondary antibody dilution and then the anti-HA antibody (1:200) was added into the remaining medium for 15-20 min (Stanika et al., 2016). Neurons were quickly but carefully washed using prewarmed HBSS (Gibco) 3 times after primary antibody incubation. Neurons were incubated in the conditioned medium containing secondary antibodies (1:200) for another 15-20 min at 37°C. After three quick washes with prewarmed HBSS, neurons were immediately fixed using ice-cold 4% paraformaldehyde containing 4% sucrose in 0.1 M Phosphate Buffer pH 7.4 for 3 min and −20°C methanol for 10 minutes. Neurons were washed with PBS three times, permeabilized with PBS containing 0.2% Triton X-100, and then incubated with blocking solution (1X PBS, 0.1%

Triton X-100 (v/v), 2.5% BSA (w/v), 5% Normal Donkey Serum (w/v), 1% glycerol (v/v)) at room temperature for 1 hour. Cells were then incubated with the blocking solution containing rabbit anti-Shank3 antibody overnight at 4°C. The following day, cells were washed three times in PBS containing 0.2% Triton X-100, then incubated with the blocking solution containing secondary antibody for 1 hour at room temperature. After washing with PBS three times, cells were mounted on slides using Prolong Gold Antifade Mountant with DAPI. Multiple lines of evidence indicate that the SHANK3 (D5K6R) Rabbit mAb (Cell Signaling, #64555) is specific: (1) The antibody was validated by western blotting in striatal synaptosomes from a Shank3 knockout mouse (https://www.cellsignal.com/products/primary-antibodies/shank3-d5k6r-rabbit-mab/64555); (2) A recent study employing three different methodologies and several Shank3 antibodies validated its use (Lutz et al., 2022); (3) Shank3 puncta were not detected when the primary antibody was omitted (data not shown), indicating that the observed staining was indeed specific to the primary antibody; and (4) The shRNA knockdown of Shank3 expression in cultured hippocampal neurons substantively reduced the signal in the soma and dendrites (Supplemental Figure 4; Figures 9 and 10).

Neuronal imaging and quantification

All neuronal imaging was performed using a 63x/1.40 Plan-APOCHROMAT oil lens as the primary objective on Zeiss LSM880 with AiryScan (Carl Zeiss Microscopy, Jena, Germany). The binocular lens was used to identify the transfected neurons based on GFP expression driven by the shRNA constructs. For whole-cell imaging, focal plane z stacks (0.3 μm steps; 1.5-2.4 μm range) were acquired. Fiji software (ImageJ, NIH) was used to merge a series of z stack images into one maximum intensity projection image.

The AiryScan module was used to maximize sensitivity and resolution for the detection of sHA-Ca_V1.3, sHA-Ca_V1.2, and endogenous Shank3 in neurons. We found that Airyscan imaging detected more abundant and somewhat smaller Shank3 puncta than conventional confocal imaging of the same neurons (Supplemental Figure 9), presumably due to the enhanced technical specifications of the Airyscan system (Wu & Hammer, 2021). The scanned area was 73.51 x 73.51 μm. Images were opened and quantified in Fiji (ImageJ, NIH). The GFP channel was used to select regions of interest (ROIs) for measuring the numbers and intensities of sHA-Ca_V1.3/sHA-Ca_V1.2 clusters. Analysis of somatic clusters was the same as in HEK cells. For dendritic analyses, 15–25 μm segments of 2-3 secondary dendrites were selected using the following criteria: (1) > 50 μm away from the soma; (2) no other crossing dendrites; (3) similar thickness. After selecting the ROI, the background was subtracted and HA signals were thresholded as for HEK cell analyses. Analyze Particles in Fiji was then used to measure the intensities, areas, and numbers of the surface localized sHA-Ca_V1.3/sHA-Ca_V1.2 clusters. In addition, a segmented line was used to measure the length of selected dendritic segments. Dendritic cluster density in each dendritic segment was calculated by dividing the total cluster number by the length, and then the average density across all dendritic segments was calculated for each neuron. A total of 6-10 neurons were analyzed per experiment, and 3-5 independent experiments were performed using different batches of neurons.

Statistical analysis

No randomization was performed to allocate treatments to the different experimental groups and no blinding was performed. Data were not assessed for normality and no tests for outliers were performed; no data points were excluded. Data are shown as mean ± SEM, and n refers to the number of cells or independent experiments, as specified in each figure legend. Statistical analyses were performed in GraphPad Prism 8 software (GraphPad, La Jolla, CA, USA). For comparisons between two groups, Student's t-test (two-tailed) or one-sample t-test was used. For comparisons between three or more samples, one-way ANOVA followed by Tukey's post hoc test was used. Comparisons between three or more groups with two independent variables were analyzed using two-way ANOVA followed by the post hoc tests recommended by Prism; all significant post hoc testing differences are defined as specific P values (correct to three decimal places) in the figures. All conditions statistically different from controls are indicated by p values labeled above columns in each figure. The complete output from Prism for each of the statistical analyses is provided in a supplementary Excel file (Supplementary Table 1).

Results

Shank3-$Ca_V1.3$ interaction requires the Shank3 PDZ domain and $Ca_V1.3$ PDZ-binding motif

Prior studies indicate that the Shank3 PDZ and SH3 domains interact directly with the C terminal-ITTL motif of $Ca_V1.3_L$ and an adjacent proline-rich region, respectively (Perfitt et al., 2020; Zhang et al., 2005). However, structural studies indicated that the Shank3 SH3 domain is atypical and has only weak (or no) interaction with multiple $Ca_V1.3$-based proline-rich peptides (Ishida et al., 2018; Ponna et al., 2017). In addition, an N-terminal extension to the Shank3 PDZ domain is critical for high-affinity interactions with GKAP (Zhou et al., 2016), but its role in binding $Ca_V1.3$ is poorly understood. Therefore, we further investigated the roles of the Shank3 SH3 and PDZ domains in interactions with $Ca_V1.3_L$.

We generated five GST-Shank3 fusion proteins containing different segments of the amino acid sequence between residue 325 (N-terminal to the SH3 domain) and residue 664 (C-terminal to the PDZ domain) (Figure 1A). GST fusion proteins (or a GST negative control) were individually incubated with lysates of HEK293T cells expressing the entire C terminal domain of the $Ca_V1.3_L$ α1 subunit preceded by an HA epitope tag (HA-$Ca_V1.3$-CTD), and protein complexes were isolated using magnetic glutathione beads (Figure 1B). We detected similar robust binding of HA-$Ca_V1.3$-CTD to the three GST-Shank3 fusion proteins containing the PDZ domain; truncation of the SH3 domain or internal deletion of residues 543-564 (N-terminal PDZ extension) had no substantial impact on the interaction. Moreover, we did not detect any interaction of the HA-$Ca_V1.3$-CTD with any fusion protein lacking the PDZ domain (containing only the SH3 domain). We then investigated interactions of a non-overlapping library of GST fusion proteins spanning the entire Shank3 protein with HA-tagged full-length $Ca_V1.3_L$ (Figure 1C). While full-length HA-$Ca_V1.3_L$ interacted with the GST-Shank3-PDZ domain, we did not detect interaction with any other GST-Shank3 fusion protein (Figure 1D). Taken together, these findings indicate that the Shank3 PDZ

domain is primarily responsible for binding to $Ca_V1.3_L$, and that the Shank3 SH3 domain has a minimal role in the interaction.

The presence of $Ca_V\beta$ subunits aids Shank3 assembly with $Ca_V1.3$ LTCCs

Although $Ca_V1.3_L$ can directly bind to the Shank3 PDZ domain, it is possible that LTCC auxiliary subunits also play a role. Therefore, we investigated the impact of $Ca_V\beta$ subunits on the interaction by performing HA co-immunoprecipitation (co-IP) experiments from lysates of HEK293T cells expressing HA-$Ca_V1.3_L$, α2δ, with or without Flag-tagged β subunits (Flag-β3 or Flag-β2a), and either GFP or GFP-Shank3. Although GFP-Shank3 co-immunoprecipitated with HA-$Ca_V1.3_L$ in the absence of β subunits, co-expression of FLAG-β3 or -β2a significantly enhanced GFP-Shank3 co-immunoprecipitation (Figure 2A, B). Interestingly, while FLAG-β3 significantly increased the co-immunoprecipitation of GFP-Shank3 by ~2-fold, FLAG-β2a had a significantly greater ~4-fold effect, even though FLAG-β3 and -β2a were expressed at similar levels. Moreover, co-expression of GFP-Shank3 increased by 2-3-fold the amounts of HA-$Ca_V1.3_L$ that were immunoprecipitated relative to the GFP control, independent of β subunit co-expression. These data indicate that Shank3 indeed associates with the full length $Ca_V1.3_L$ and that β subunits may stabilize the interaction.

To further explore the role of β subunits in $Ca_V1.3$-Shank3 interaction, we incubated lysates of HEK293T cells expressing HA-$Ca_V1.3$ and α2δ with or without β3 or β2a with GST or GST-Shank3-PDZ. As seen in Figure 1A, HA-$Ca_V1.3$ associated with GST-Shank3-PDZ on magnetic glutathione beads in the absence of β subunits. However, co-expression of either FLAG-β2a or FLAG-β3 had no significant impact on the amount of HA-$Ca_V1.3$ that associated with GST-Shank3-PDZ (Figure 2D, E). These data indicate that the direct interaction of the $Ca_V1.3$ α1 subunit C-terminal domain with the Shank3 PDZ domain is unaffected by β subunits, suggesting that the ability of β subunits to enhance full-length Shank3 co-immunoprecipitation with full length $Ca_V1.3$ (Figure 2A, B) requires other domains in Shank3.

To test the hypothesis that Shank3 may interact with LTCC β subunits in the absence of $Ca_V1.3$, we co-expressed FLAG-β3 or -β2a in HEK293T cells with either full-length GFP-Shank3, GFP-Shank3-ΔPDZ (internal deletion of the PDZ domain) or a GFP control. Immunoprecipitation using an anti-GFP antibody revealed that significantly more FLAG-β3 than FLAG-β2a associated with full length GFP-Shank3, and that deletion of the Shank3 PDZ domain had little effect on this interaction (Figure 3A, B). However, reciprocal immunoprecipitations using a FLAG antibody indicated that similar amounts of full length GFP-Shank3 associated with FLAG-β3 or FLAG-β2a. The amount of GFP-Shank3 associated with both FLAG-β3 and FLAG-β2a appeared to be reduced by deletion of the PDZ domain (Figure 3C, D), but the reduction was not statistically significant in post hoc tests (Supplementary Table 1). In an effort to determine which domains in Shank3 are sufficient for β subunit binding, we investigated the interaction of full-length FLAG-β3 or FLAG-β2a with our family of GST-Shank3 fusion proteins (Figure 1C). However, we failed to detect interactions of either FLAG-β3 or FLAG-β2a with any of the GST-Shank3 fusion proteins (Supplemental Figure 1). Taken together, these data indicate that LTCC β

subunits can associate with Shank3 independent of the $Ca_V1.3$ α1 subunit, and that this interaction does not strictly require the Shank3 PDZ domain, although there may be some modest quantitative effects. The interaction of Shank3 with β subunits may contribute to β subunit-dependent enhancement of Shank3 association with full-length $Ca_V1.3$ observed in Figures 2A and 2B.

The Shank3 PDZ domain mediates assembly of complexes containing multiple $Ca_V1.3_L$ LTCCs

The amount of HA-$Ca_V1.3_L$ immunoprecipitated using an HA antibody was consistently increased by GFP-Shank3 co-expression, independent of the β subunit (Figure 2C). Since the HA antibody immunoprecipitated only a fraction of the total HA-$Ca_V1.3_L$ from these lysates, we hypothesized that this might be due to the clustering of multiple HA-$Ca_V1.3_L$ subunits by Shank3 multimers (Naisbitt et al., 1999). To directly test this hypothesis (Figure 4A), we co-expressed mCherry-tagged $Ca_V1.3_L$ (mCherry-$Ca_V1.3_L$) and HA-$Ca_V1.3_L$, along with α2δ and FLAG-β2a subunits and either GFP, GFP-Shank3, or GFP-Shank3-ΔPDZ. GFP-Shank3 specifically and efficiently co-precipitated with HA-$Ca_V1.3_L$ relative to the GFP control, and deletion of the PDZ domain significantly reduced the co-immunoprecipitation by ~80% (Figure 4B, C). Presumably, the residual co-immunoprecipitation of GFP-Shank3-ΔPDZ with HA-$Ca_V1.3_L$ is mediated by the β2a subunit. Notably, mCherry-$Ca_V1.3$ was readily detected in HA-immune complexes isolated from cells co-expressing GFP-Shank3, but only low levels of mCherry-$Ca_V1.3$ were detected in complexes isolated from cells co-expressing GFP or GFP-Shank3-ΔPDZ (Figure 4B, D). These data provide direct biochemical support for the hypothesis that Shank3 can cluster multiple $Ca_V1.3_L$ in a complex and that the PDZ domain is crucial for this clustering.

Shank3-dependent clustering of $Ca_V1.3_L$ *in vitro* is disrupted by Ca^{2+} addition.

Next, we tested whether the assembly of mCherry-$Ca_V1.3_L$ with HA-$Ca_V1.3_L$ was affected by Ca^{2+} or CaM. Lysates of cells co-expressing mCherry-$Ca_V1.3_L$, HA-$Ca_V1.3_L$, α2δ and FLAG-β2a subunits with either GFP or GFP-Shank3 were HA-immunoprecipitated under basal conditions (with EDTA) or following the addition of Ca^{2+}/CaM (Figure 5A). In GFP control cell lysates, the addition of Ca^{2+}/CaM slightly increased the amount of mCherry-$Ca_V1.3$ detected in the HA-immune complexes in 5 out of 6 experiments, but the average ~1.5-fold increase was not statistically significant. As seen in Figure 4, the co-expression of GFP-Shank3 significantly increased the levels of mCherry-$Ca_V1.3_L$ detected in HA-immune complexes under basal (EDTA) conditions, but the addition of Ca^{2+}/CaM significantly reduced the levels of co-precipitated mCherry-$Ca_V1.3_L$ (Figure 5B). Moreover, Ca^{2+}/CaM addition also significantly reduced the levels of GFP-Shank3 that co-precipitated with HA-$Ca_V1.3_L$ (Figure 5C). These data demonstrate that the Shank3-dependent assembly of complexes containing multiple $Ca_V1.3$ α1 subunits can be disrupted by adding Ca^{2+}/CaM to cell lysates.

To explore whether Ca^{2+} alone or Ca^{2+}-activated CaM is required for these effects, lysates of cells co-expressing mCherry-$Ca_V1.3_L$, HA-$Ca_V1.3_L$, α2δ and FLAG-β3 subunits with GFP-Shank3 were HA-immunoprecipitated with the addition of Ca^{2+} alone, CaM alone, or Ca^{2+} plus CaM, or with no addition (Figure 5D). Consistent with Figure 5A, Ca^{2+}/CaM

addition significantly reduced the levels of Shank3 and mCherry-$Ca_V1.3_L$ in immune complex. Similar effects were observed following the addition of Ca^{2+} alone, but not following the addition of CaM alone. In order to investigate whether the effects of adding Ca^{2+} alone were mediated by CaM that is endogenous to the cell lysates, these experiments were repeated in the presence of calmidazolium (50 μM), a widely used CaM antagonist (Figure 5D-5F). However, calmidazolium had no effect on the co-immunoprecipitation of Shank3 or mCherry-$Ca_V1.3_L$ with HA-$Ca_V1.3_L$ under any of these conditions (Figure 5E and 5F). Importantly, we confirmed that calmidazolium was an effective CaM antagonist by showing that it blocked Ca^{2+}/CaM-dependent CaMKII autophosphorylation at Thr286 *in vitro* (Supplemental Figure 2). Taken together, these data indicate that Ca^{2+} directly interferes with Shank3-binding and $Ca_V1.3$ clustering, independent of CaM.

Shank3 stabilizes $Ca_V1.3$ LTCCs in the plasma membrane under basal conditions *in situ*

As an initial test of the hypothesis that Shank3 clusters $Ca_V1.3_L$ in the plasma membrane, we used TIRF microscopy to detect fluorescent proteins residing within ~100 nm of the cover slip in live HEK293 cells co-expressing mCherry-$Ca_V1.3_L$, α2δ and β2a/β3 subunits with either GFP or GFP-Shank3. We detected mCherry puncta in cells co-expressing GFP-Shank3, or the GFP control (Figure 6A), presumably predominantly reflecting LTCCs that had been trafficked to the plasma membrane. Moreover, GFP-Shank3 strongly colocalized with many of the mCherry-$Ca_V1.3_L$ puncta (Figure 6A). Notably, mCherry puncta were significantly more intense in cells expressing GFP-Shank3 than in GFP control cells (Figure 6B), consistent with the hypothesis that GFP-Shank3 increases the number of mCherry-tagged α1 subunits within each puncta. Repeated imaging of these cells over 3-5 minutes indicated that mCherrry-$Ca_V1.3_L$ clusters generally appeared transiently in TIRF images of GFP control cells (Figure 6Ai), whereas in the presence of GFP-Shank3 most mCherry-$Ca_V1.3_L$ puncta in the TIRF images remained for the duration of the imaging session (Figure 6Aii). Moreover, mCherry-$Ca_V1.3_L$ puncta were quite motile within the plane of the plasma membrane in GFP control cells, moving at average speeds of ~0.25 μm/s, whereas in cells expressing GFP-Shank3 they moved significantly slower (~0.1 μm/s) (Figure 6D). Figures 6C and 6D summarize data from multiple experiments co-expressing either FLAG-β3 (solid symbols) or FLAG-β2a (open symbols), indicating that the impact of GFP-Shank3 on mCherry-$Ca_V1.3_L$ appears to be independent of the identity of the β subunit. Taken together, these data are consistent with a model in which Shank3 stabilizes $Ca_V1.3_L$ α1 subunit clusters in HEK293 cell plasma membranes.

The Shank3 PDZ domain mediates basal $Ca_V1.3$ clustering in intact cells

We next tested for an effect of LTCC-mediated Ca^{2+} influx on mCherry-$Ca_V1.3$ in live HEK293 cells co-expressing GFP-Shank3. LTCCs were activated pharmacologically using Bay K8644 (BayK) (10 μM) in the absence or presence of added extracellular Ca^{2+} while monitoring plasma membrane localized mCherry-$Ca_V1.3_L$ and GFP-Shank3 in single HEK293 cells by live-cell TIRF imaging. After collecting baseline data in a 0 mM Ca^{2+} buffer, cells were switched to 0 mM Ca^{2+} buffer with BayK for several minutes, and then to 2.5 mM Ca^{2+} buffer with BayK. Figure 7A shows a single representative cell at t=0, and marks a region of interest containing co-localized mCherry-$Ca_V1.3_L$/GFP-Shank3 clusters. The ratio of mCherry/GFP fluorescence in this region of interest was measured

at 5 s intervals and plotted in Figure 7B under each of the buffer conditions, with about a one-minute gap as the buffer solutions were switched; the insets show images of the region of interest at selected time points. The mCherry/GFP ratio was relatively stable throughout the incubation with 0 Ca^{2+}, in the absence or presence of BayK. However, addition of the Ca^{2+}/BayK buffer decreased the mCherry/GFP ratio within one minute of the buffer exchange, mainly due to a substantial reduction in the mCherry-$Ca_V1.3_L$ intensity (Figure 7C). Figure 7D shows the mCherry/GFP ratio from 12 cells co-expressing either FLAG-β3 (solid symbols) or FLAG-β2a (open symbols; Supplemental Figure 3) in each of the three buffer conditions, normalized to the 0 Ca^{2+} buffer, indicating that Ca^{2+} influx significantly reduces the intensity of mCherry-$Ca_V1.3_L$ clusters colocalized with GFP-Shank3.

In order to provide further insight into the role of Shank3 in $Ca_V1.3$ LTCC clustering *in situ*, HEK293 cells expressing mCherry-$Ca_V1.3$ and either GFP, GFP-Shank3, or GFP-Shank3-ΔPDZ were incubated for 10-15 min in a HEPES buffer supplemented with 0 or 2.5 mM Ca^{2+}, in the absence or presence of BayK (Figure 8A), and then fixed for imaging using a TIRF microscope. As seen in live HEK293 cells (Figures 6 and 7), mCherry-$Ca_V1.3_L$ puncta were readily detected near the cell surface under all conditions, and we quantified the puncta intensity (Figure 8B) and density (Figure 8C). In cells co-expressing GFP (gray circles/bars), both parameters were unaffected by incubation of the cells with or without extracellular Ca^{2+} and/or BayK. The co-expression of GFP-Shank3 significantly increased the intensity of mCherry-$Ca_V1.3_L$ puncta by ~2-fold (blue squares/bars) when cells were incubated in the absence of extracellular Ca^{2+} (+/− BayK) or with Ca^{2+} in the absence of BayK. However, incubation of cells expressing GFP-Shank3 with both Ca^{2+} and BayK significantly reduced the mCherry-$Ca_V1.3_L$ puncta intensity to levels observed in GFP control cells. Notably, GFP-Shank3 co-expression had no effect on the mCherry-$Ca_V1.3_L$ puncta density, and the puncta density in cells expressing GFP-Shank3 was unaffected by the Ca^{2+}/BayK incubations. Importantly, the co-expression of GFP-Shank3-ΔPDZ (red triangles/bars) had no significant effect on the intensity or density of mCherry-$Ca_V1.3_L$ puncta compared to the GFP control under any condition tested.

In parallel, we quantified the co-localization of GFP signals with mCherry-$Ca_V1.3_L$ using the ICQ method (Figure 8D). The ICQ score in cells co-expressing soluble GFP and mCherry-$Ca_V1.3_L$ was very low (~0.05) under all conditions, as expected for mostly random overlap. In contrast, GFP-Shank3 significantly colocalized with mCherry-$Ca_V1.3_L$ puncta (ICQ ~0.25) when cells were pre-incubated in the absence of extracellular Ca^{2+} (+/− BayK) or with Ca^{2+} in the absence of BayK. However, the simultaneous addition of Ca^{2+} and BayK significantly decreased the ICQ to ~0.15. Moreover, GFP-Shank3-ΔPDZ was only weakly co-localized with mCherry-$Ca_V1.3_L$ (ICQ ~ 0.15), independent of the specific cell incubation condition. Taken together, these data indicate that the Shank3 PDZ domain is essential for efficient colocalization with $Ca_V1.3$, and also for efficient $Ca_V1.3$ clustering under basal conditions, and that LTCC-mediated Ca^{2+} influx disrupts the effect of Shank3.

Endogenous Shank3 clusters $Ca_V1.3_L$ in cultured hippocampal neurons

Previous over-expression studies in cultured neurons indicated that Shank3 interaction with the $Ca_V1.3$ C-terminal domain facilitates $Ca_V1.3$ LTCC surface expression in dendrites

(Stanika et al., 2016; Zhang et al., 2006). However, the role of endogenous Shank3 has not been investigated. Therefore, we expressed $Ca_V1.3_L$ with an extracellular HA tag (sHA-$Ca_V1.3$), α2δ and either FLAG-β3 or -β2a, with or without a well-characterized highly effective and specific shRNA to knock down endogenous Shank3 expression (Perfitt et al., 2020; Verpelli et al., 2011). First, using a well validated antibody to stain for endogenous Shank3 (see Methods), we confirmed the efficacy of Shank3 knockdown in DIV21 neurons that were co-transfected to express the LTCC subunits at DIV14. In non-transfected neurons (NT) or neurons expressing control nonsense shRNA (nssh), punctate staining for endogenous Shank3 was readily detected in the soma and dendrites (Supplemental Figure 4A), consistent with previous studies (Lutz et al., 2022; Perfitt et al., 2020; Wu et al., 2022; Zhang et al., 2005). Moreover, the intensity of somatic Shank3 puncta was essentially identical in non-transfected neurons and neurons expressing the control RNA (nssh/NT ratios: 1.19±0.14 and 1.14±0.12 in neurons co-expressing β3 and β2a subunits, respectively) (Supplemental Figure 4B). However, expression of the Shank3-shRNA (SK3-sh) significantly reduced the intensity of endogenous Shank3 fluorescence by ~80% (SK3-sh/NT ratios: 0.28±0.04 and 0.17±0.03 in neurons co-expressing β3 and β2a subunits, respectively) (Supplemental Figure 4B). The high density of overlapping non-transfected dendrites in these cultures/images precluded accurate quantification of dendritic Shank3 levels in transfected neurons. These data confirm that the shRNA reliably knocked down Shank3 protein expression under the current experimental conditions, albeit with somewhat reduced efficacy than we observed previously in younger neurons (Perfitt et al., 2020).

We then examined the impact of Shank3 knockdown on sHA-$Ca_V1.3$ cell surface expression. Consistent with previous studies (Moreno et al., 2016; Stanika et al., 2016; Zhang et al., 2016), live cell labelling revealed a clustered distribution of surface localized sHA-$Ca_V1.3_L$ channels on the soma and dendrites (Figure 9A). To test the specificity of surface labeling, a Z-stack series of images were collected: X-Z and Y-Z dimension projection images showed that HA clusters were excluded from within the soma (Supplemental Figure 8). In neurons expressing control shRNA, sHA-$Ca_V1.3_L$ clusters were partially colocalized with endogenous Shank3 on the soma and dendrites (Figure 9A and Supplemental Figure 10). Notably, the robust Shank3 knockdown significantly decreased the average intensity of sHA-$Ca_V1.3_L$ clusters in neuronal dendrites, when expressed with either FLAG-β3 (Figure 9C and Supplemental Figure 5B) or FLAG-β2a (Supplemental Figure 6C). However, there was only a trend for a decrease of somatic sHA-$Ca_V1.3_L$ cluster intensity (Figure 9B, Supplemental Figure 5A, and Supplemental Figure 6B). In contrast, Shank3 knockdown significantly reduced the density (number) of both somatic and dendritic sHA-$Ca_V1.3_L$ clusters when expressed with either FLAG-β3 (Figure 9B, C) or FLAG-β2a (Supplemental Figure 6). To explore if Shank3 specifically affects $Ca_V1.3_L$ LTCC clustering, we examined $Ca_V1.2$ LTCC cell surface expression with or without Shank3 knockdown (Figure 10). The sHA-$Ca_V1.2$ clusters were not strongly colocalized with endogenous Shank3 in control cells (Figure 10A and Supplemental Figure 10), as expected because the $Ca_V1.2$ α1 subunit does not directly interact with Shank3 (Zhang et al., 2005). Consistent with these findings, Shank3 knockdown had no significant effect on the intensity or the density of dendritic sHA-$Ca_V1.2$ clusters. Similarly, Shank3 knockdown had no effect on the intensity of somatic $Ca_V1.2$ clusters, although the density of somatic

$Ca_V1.2$ clusters was modestly, but significantly, reduced (Figure 10B, C and Supplemental Figure 7A, B). In combination, these data indicate that endogenous Shank3 plays an important and specific role in the dendritic clustering and overall surface expression of $Ca_V1.3_L$ LTCCs under basal conditions.

Discussion

Here we significantly extend prior studies to provide new insights into the role of Shank3 in controlling $Ca_V1.3$ LTCC clustering. Complementary co-immunoprecipitation and fluorescence microscopy studies using heterologous cells demonstrate that a direct interaction between the C-terminal domain of the $Ca_V1.3$ α1 subunit and the PDZ domain of Shank3 can mediate the clustering of multiple $Ca_V1.3$ LTCCs. Our data also indicate that LTCC β3 or β2a auxiliary subunits facilitate Shank3 clustering of $Ca_V1.3$ LTCCs, perhaps by directly (or indirectly) interacting with Shank3 independent of the $Ca_V1.3$ α1 subunit. Significantly, our data indicate Shank3-$Ca_V1.3$ association and Shank3-dependent $Ca_V1.3$ clustering can be disrupted by increasing Ca^{2+}, indicating that $Ca_V1.3$ clustering can be dynamically modulated by LTCC activation. Finally, we showed that Shank3 knockdown disrupted dendritic $Ca_V1.3$ clustering in cultured hippocampal neurons. Taken together, our data substantially advance our understanding of the role of Shank3 in $Ca_V1.3$ LTCC clustering.

The Shank3 PDZ domain mediates $Ca_V1.3_L$ LTCC clustering under basal conditions

Shank proteins are multi-domain scaffolding proteins localized to excitatory synapses, where they coordinate the assembly of several multiprotein complexes (Naisbitt et al., 1999; Sheng & Hoogenraad, 2007; Sheng & Kim, 2000). It is well established that Shank PDZ domains can interact with multiple synaptic proteins, and deletion of the Shank3 PDZ domain in mice results in synaptic dysfunction and autism-related behavioral phenotypes (Peça et al., 2011), demonstrating the importance of interactions with the Shank3 PDZ domain.

Here, our *in vitro* studies using GST fusion proteins showed that the Shank3 PDZ domain is necessary and sufficient for binding to the C-terminal domain of $Ca_V1.3_L$ or to the full length $Ca_V1.3_L$ α1 subunit. In contrast to a prior report (Zhang et al., 2005), our data provided no indication that the Shank3 SH3 domain plays a significant role in this interaction. The reasons for this discrepancy are unclear, but it is possible that a low affinity interaction of $Ca_V1.3_L$ with the SH3 domain (Ishida et al., 2018) could not be detected under our experimental conditions. These *in vitro* studies also indicated that β auxiliary subunits had a hitherto unappreciated role in facilitating Shank3 interactions with $Ca_V1.3_L$ LTCCs, apparently by also interacting with Shank3. However, preliminary *in vitro* studies (Supplementary Figure 1) failed to detect a direct interaction of either β2a or β3 with the PDZ domain or any other tested fragment of Shank3. Alternatively, if Shank3 preferentially interacts with $Ca_V1.3_L$ in the plasma membrane, it is possible that β subunits enhance the interaction by facilitating the trafficking of $Ca_V1.3_L$ to the membrane, as previously shown (Altier et al., 2011; Bourdin et al., 2010; Obermair et al., 2010). Further studies are required to define the mechanism underlying the effects of the β subunit on the interaction between Shank3 and $Ca_V1.3$.

We then adapted our co-immunoprecipitation assay to detect interactions between co-expressed $Ca_V1.3_L$ LTCCs with different epitope tags, demonstrating that Shank3 can mediate the assembly of complexes containing multiple $Ca_V1.3_L$ LTCCs, and that the Shank3 PDZ domain is essential for assembly of these complexes. We extended these studies to investigate the impact of Shank3 on $Ca_V1.3_L$ clustering in the plasma membrane of heterologous (HEK293) cells. TIRF microscopy provided no evidence that co-expression of Shank3 modulated cell surface expression levels ($Ca_V1.3_L$ puncta density) in HEK293 cells under basal cell incubation conditions. Rather, we found that Shank3 expression increased the average intensity (or brightness) of cell surface $Ca_V1.3_L$ puncta in both live-cell imaging studies (Figure 6) and in fixed cells (Figure 7). We interpret the increased signal intensity/brightness as an increase of the average number of mCherry-$Ca_V1.3_L$ α1 subunits within each puncta, or $Ca_V1.3_L$ LTCC clustering, and this increase was also dependent on the Shank3 PDZ domain. Prior cell biology studies have indicated that $Ca_V1.3_S$ and $Ca_V1.3_L$ variants can “self-cluster” in the plasma membrane, with each cluster containing an average of ~8 α1 subunits (Moreno et al., 2016). However, $Ca_V1.3_S$ lacks the PDZ binding C-terminal ITTL motif that mediates $Ca_V1.3_L$ with the Shank3 PDZ domain, and therefore cannot interact with Shank3 (Zhang et al., 2005). Thus, the Shank3-dependent clustering observed in our co-immunoprecipitation and cell imaging studies may represent a specific mechanism for higher-order clustering of $Ca_V1.3_L$.

Previous studies found that Shank3 and surface expressed $Ca_V1.2/1.3$ adopt a punctate distribution in the soma and dendrites of cultured neurons, but these puncta are not exclusively synaptic, even in dendrites (Folci et al., 2018; Lutz et al., 2022; Obermair et al., 2004; Stanika et al., 2016). A prior study found that endogenous synaptic Shank3 puncta appear to be somewhat larger on average than extra-synaptic dendritic Shank3 puncta (Lutz et al., 2022), consistent with the idea that the composition of Shank3 complexes depends on their subcellular location. In addition, $Ca_V1.3$, but not $Ca_V1.2$, interacts with Shank3 *in vitro* (Zhang et al., 2005), consistent with our observation that endogenous Shank3 co-localizes with sHA-$Ca_V1.3$ more strongly than with sHA-$Ca_V1.2$ (Supplemental Figure 10). Low levels of $Ca_V1.2$ colocalization with Shank3 may be due to synaptic targeting of $Ca_V1.2$ via other mechanisms resulting in apparent overlap with synaptic pools of Shank3 because the actual physical size of these structures is at or below the resolution limit of the microscope. Most importantly, we found that knocking down Shank3 expression in cultured neurons had a significant impact on $Ca_V1.3_L$ (Figure 9) but not $Ca_V1.2$ (Figure 10) in the plasma membrane. Shank3 knockdown significantly decreased the overall density of cell surface $Ca_V1.3_L$ puncta in both the soma and dendrites, indicating that Shank3 enhances cell surface expression of $Ca_V1.3_L$ LTCCs in neurons. Similar decreases in density were observed in neurons that co-expressed $Ca_V1.3_L$ with either the β2a or β3 subunits. These findings are consistent with prior reports indicating that Shank3 enhances $Ca_V1.3_L$ trafficking to the neuronal plasma membrane (Zhang et al., 2006). Shank3 knockdown also significantly decreased the intensity of surface $Ca_V1.3_L$ puncta in neuronal dendrites, but not in the soma, once again irrespective of the identity of the co-expressed β subunit. These observations indicate an additional dendritic role for Shank3 in increasing the number of $Ca_V1.3_L$ α1 subunits within each puncta. Moreover, the observed changes in sHA-$Ca_V1.3$ staining following knockdown of Shank3 expression are consistent with our biochemical

and heterologous cell studies and are not observed with sHA-$Ca_V1.2$. These observations support the hypothesis that endogenous Shank3 specifically promotes the clustering of $Ca_V1.3_L$ LTCCs in neuronal dendrites under basal culture conditions.

Shank3 binding and $Ca_V1.3_L$ clustering is disrupted in the presence of Ca^{2+}

We also hypothesized that $Ca_V1.3_L$ clustering might be sensitive to increased Ca^{2+}. Neuronal depolarization has been shown to enhance the physical and/or functional coupling of $Ca_V1.2$ and $Ca_V1.3_S$ LTCCs (Dixon et al., 2015; Moreno et al., 2016), and some data indicate that Ca^{2+}/CaM can induce homodimerization of $Ca_V1.2$ LTCCs (Fallon et al., 2009). A recent modeling study estimated that free Ca^{2+} concentrations in nanodomains formed from a single activated voltage-gated calcium channel are ~ 500 μM at the mouth of the channel, dropping to ~60 μM and ~18 μM at 20 nm and 100 nm from the channel (Nakamura et al., 2018). We found that adjusting HEK293T cell lysates to ~200 μM free Ca^{2+} (see methods) dissociated Shank3 from $Ca_V1.3_L$ complexes and disrupted Shank-3 dependent co-immunoprecipitation of HA- and mCherry-tagged $Ca_V1.3_L$ (Figure 5). Interestingly, although we initially hypothesized that calmodulin would mediate this effect, perhaps via interactions with the N- and/or C-terminal domain of $Ca_V1.3_L$ (Ben Johny et al., 2013; Moreno et al., 2016), we found that calmidozolium (a calmodulin antagonist) had no effect on the ability of Ca^{2+} to disrupt the co-immunoprecipitated complex.

In studies exploring the impact of Shank3 and Ca^{2+} on $Ca_V1.3_L$ clustering in HEK293 cells, we found that the Shank3 enhanced clustering $Ca_V1.3_L$ LTCCs on plasma membranes under basal conditions (see above) was disrupted following LTCC activation using BayK8644 in the presence, but not the absence, of extracellular Ca^{2+} (Figures 7 and 8). Since BayK was previously shown to induce Ca^{2+} influx into heterologous cells under similar conditions (Tian et al., 2008), our data indicate that Shank3-binding and $Ca_V1.3_L$ clustering are disrupted by Ca^{2+} influx via the LTCC itself, but not by BayK8644-induced conformational changes in $Ca_V1.3_L$ (Marom et al., 2010) or Ca^{2+} influx via other mechanisms. Further studies will be required to elucidate the mechanisms underlying Ca^{2+}-dependent disruption of Shank3 binding and $Ca_V1.3_L$ clustering.

The potential roles of $Ca_V1.3$ channel clustering

Activation of neuronal LTCCs has been suggested to create local Ca^{2+} nanodomains near the plasma membrane that have privileged roles in initiating downstream signaling cascades, such as E-T coupling (Deisseroth et al., 1996; Wheeler et al., 2012). It seems likely that the clustering of multiple LTCCs within a single complex facilitates the formation of larger Ca^{2+} nanodomains that may attain higher Ca^{2+} concentrations, enhancing downstream signaling. In support of this notion, several different experimental approaches have indicated that Shank3 has a key role in facilitating $Ca_V1.3$ LTCC-induced excitation-transcription coupling (see Introduction). We suggest that this facilitation of E-T coupling is due to the Shank3-dependent $Ca_V1.3_L$ clustering reported here. Although it may seem somewhat paradoxical that Shank3-dependent $Ca_V1.3_L$ clustering is disrupted by Ca^{2+} influx, several other mechanisms undoubtedly contribute to the control of LTCC clustering and the dynamics of Ca^{2+} nanodomains. For example, clustering of $Ca_V1.3_S$ channels (which cannot bind

Shank3) enhances Ca^{2+} influx by allowing for Ca^{2+}/CaM-dependent functional coupling within the cluster (Moreno et al., 2016). However, even though $Ca_V1.3_L$ LTCCs form clusters with similar biophysical characteristics, they do not seem to be regulated by this Ca^{2+}/CaM-dependent functional coupling mechanism. Further studies will be required to develop a deeper understanding of the molecular mechanisms controlling the regulation of $Ca_V1.3$ splice variant clustering and the physiological significance of clustering. Since genetic variants of Shank3 and LTCCs in humans are being increasingly linked to autism spectrum disorders, schizophrenia and other neuropsychiatric disorders (Gauthier et al., 2010; Guilmatre et al., 2014; Martínez-Rivera et al., 2017; Monteiro & Feng, 2017; Pinggera et al., 2015), such studies also may provide insight into the pathophysiology of these disorders.

Supplementary Material

Refer to Web version on PubMed Central for supplementary material.

--Acknowledgments--

This work was funded by National Institute of Diabetes and Digestive and Kidney Diseases, (Grant / Award Number: 'T32DK007563')

American Heart Association, (Grant / Award Number: '18PRE33960034') (grant number): This information is usually included already, but please add to the Acknowledgments if not.

Acknowledgements

This work was supported by Vanderbilt University and an endowed Louise B. McGavock Chair to R.J.C., and by an AHA fellowship 18PRE33960034 to T.L.P. Confocal imaging and analysis were performed in part through the use of the Vanderbilt Cell Imaging Shared Resource (supported by National Institutes of Health Grants CA68485, DK20593, DK58404, DK59637, and EY08126). The content is solely the responsibility of the authors and does not necessarily represent the official views of the National Institutes of Health. We thank Drs. Craig Garner, Gerald Zamponi, Luk Van Parijs, and Diane Lipscombe for generously providing various original plasmids, as detailed in Key Resources Table.

Data Availability Statement

A preprint of this article was published on BioRxiv on 22-Oct-2022: https://www.biorxiv.org/content/10.1101/2022.10.21.513252v1

Abbreviations

ANK	ankyrin-rich repeats
CaM	Calmodulin
CaMKII	Calcium/calmodulin-dependent protein kinase II
CTD	C-terminal domain
E-T coupling	excitation-transcription coupling
GFP	enhanced green fluorescent protein
GST	Glutathione-S-transferase

HA	Hemagglutinin
ICQ	intensity correlation quotient
LTCC	L-type calcium channel
nssh	nonsense-shRNA
PDZ domain	PSD95/DlgA/Zo-1 domain
PPR	proline-rich region
SAM	Sterile alpha motif
SH3	Src homology 3 domain
TIRF	Total internal reflection fluorescence
WT	wild type

References

Abiria SA, & Colbran RJ (2010). CaMKII associates with CaV1.2 L-type calcium channels via selected beta subunits to enhance regulatory phosphorylation. J Neurochem, 112(1), 150–161. 10.1111/j.1471-4159.2009.06436.x [PubMed: 19840220]

Altier C, Dubel SJ, Barrère C, Jarvis SE, Stotz SC, Spaetgens RL, … Bourinet E (2002). Trafficking of L-type calcium channels mediated by the postsynaptic scaffolding protein AKAP79. J Biol Chem, 277(37), 33598–33603. 10.1074/jbc.M202476200 [PubMed: 12114507]

Altier C, Garcia-Caballero A, Simms B, You H, Chen L, Walcher J, … Zamponi GW (2011). The Cavβ subunit prevents RFP2-mediated ubiquitination and proteasomal degradation of L-type channels. Nat Neurosci, 14(2), 173–180. 10.1038/nn.2712 [PubMed: 21186355]

Bartlett RK, Bieber Urbauer RJ, Anbanandam A, Smallwood HS, Urbauer JL, & Squier TC (2003). Oxidation of Met144 and Met145 in calmodulin blocks calmodulin dependent activation of the plasma membrane Ca-ATPase. Biochemistry, 42(11), 3231–3238. 10.1021/bi026956z [PubMed: 12641454]

Ben Johny M, Yang PS, Bazzazi H, & Yue DT (2013). Dynamic switching of calmodulin interactions underlies Ca2+ regulation of CaV1.3 channels. Nat Commun, 4, 1717. 10.1038/ncomms2727 [PubMed: 23591884]

Bock G, Gebhart M, Scharinger A, Jangsangthong W, Busquet P, Poggiani C, … Koschak A (2011). Functional properties of a newly identified C-terminal splice variant of Cav1.3 L-type Ca2+ channels. J Biol Chem, 286(49), 42736–42748. 10.1074/jbc.M111.269951 [PubMed: 21998310]

Boudkkazi S, Brechet A, Schwenk J, & Fakler B (2014). Cornichon2 dictates the time course of excitatory transmission at individual hippocampal synapses. Neuron, 82(4), 848–858. 10.1016/j.neuron.2014.03.031 [PubMed: 24853943]

Bourdin B, Marger F, Wall-Lacelle S, Schneider T, Klein H, Sauvé R, & Parent L (2010). Molecular determinants of the CaVbeta-induced plasma membrane targeting of the CaV1.2 channel. J Biol Chem, 285(30), 22853–22863. 10.1074/jbc.M110.111062 [PubMed: 20478999]

Calin-Jageman I, Yu K, Hall RA, Mei L, & Lee A (2007). Erbin enhances voltage-dependent facilitation of Ca(v)1.3 Ca2+ channels through relief of an autoinhibitory domain in the Ca(v)1.3 alpha1 subunit. J Neurosci, 27(6), 1374–1385. 10.1523/JNEUROSCI.5191-06.2007 [PubMed: 17287512]

Catterall WA (2011). Voltage-gated calcium channels. Cold Spring Harb Perspect Biol, 3(8), a003947. 10.1101/cshperspect.a003947 [PubMed: 21746798]

Costé de Bagneaux P, Campiglio M, Benedetti B, Tuluc P, & Flucher BE (2018). Role of putative voltage-sensor countercharge D4 in regulating gating properties of Ca. Channels (Austin), 12(1), 249–261. 10.1080/19336950.2018.1482183 [PubMed: 30001160]

Deisseroth K, Bito H, & Tsien RW (1996). Signaling from synapse to nucleus: postsynaptic CREB phosphorylation during multiple forms of hippocampal synaptic plasticity. Neuron, 16(1), 89–101. 10.1016/s0896-6273(00)80026-4 [PubMed: 8562094]

Dittgen T, Nimmerjahn A, Komai S, Licznerski P, Waters J, Margrie TW, … Osten P (2004). Lentivirus-based genetic manipulations of cortical neurons and their optical and electrophysiological monitoring in vivo. Proc Natl Acad Sci U S A, 101(52), 18206–18211. 10.1073/pnas.0407976101 [PubMed: 15608064]

Dixon RE, Moreno CM, Yuan C, Opitz-Araya X, Binder MD, Navedo MF, & Santana LF (2015). Graded Ca^{2+}/calmodulin-dependent coupling of voltage-gated CaV1.2 channels. Elife, 4. 10.7554/eLife.05608

Dixon RE, Yuan C, Cheng EP, Navedo MF, & Santana LF (2012). Ca2+ signaling amplification by oligomerization of L-type Cav1.2 channels. Proc Natl Acad Sci U S A, 109(5), 1749–1754. 10.1073/pnas.1116731109 [PubMed: 22307641]

Fallon JL, Baker MR, Xiong L, Loy RE, Yang G, Dirksen RT, … Quiocho FA (2009). Crystal structure of dimeric cardiac L-type calcium channel regulatory domains bridged by Ca2+* calmodulins. Proc Natl Acad Sci U S A, 106(13), 5135–5140. 10.1073/pnas.0807487106 [PubMed: 19279214]

Folci A, Steinberger A, Lee B, Stanika R, Scheruebel S, Campiglio M, … Di Biase V (2018). Molecular mimicking of C-terminal phosphorylation tunes the surface dynamics of $Ca_V1.2$ calcium channels in hippocampal neurons. J Biol Chem, 293(3), 1040–1053. 10.1074/jbc.M117.799585 [PubMed: 29180451]

Gauthier J, Champagne N, Lafrenière RG, Xiong L, Spiegelman D, Brustein E, … Team, S. D. (2010). De novo mutations in the gene encoding the synaptic scaffolding protein SHANK3 in patients ascertained for schizophrenia. Proc Natl Acad Sci U S A, 107(17), 7863–7868. 10.1073/pnas.0906232107 [PubMed: 20385823]

Gopalakrishna R, & Anderson WB (1982). Ca2+-induced hydrophobic site on calmodulin: application for purification of calmodulin by phenyl-Sepharose affinity chromatography. Biochem Biophys Res Commun, 104(2), 830–836. 10.1016/0006-291x(82)90712-4 [PubMed: 6803791]

Gregory FD, Bryan KE, Pangršič T, Calin-Jageman IE, Moser T, & Lee A (2011). Harmonin inhibits presynaptic Cav1.3 Ca^{2+} channels in mouse inner hair cells. Nat Neurosci, 14(9), 1109–1111. 10.1038/nn.2895 [PubMed: 21822269]

Guilmatre A, Huguet G, Delorme R, & Bourgeron T (2014). The emerging role of SHANK genes in neuropsychiatric disorders. Dev Neurobiol, 74(2), 113–122. 10.1002/dneu.22128 [PubMed: 24124131]

Hui A, Ellinor PT, Krizanova O, Wang JJ, Diebold RJ, & Schwartz A (1991). Molecular cloning of multiple subtypes of a novel rat brain isoform of the alpha 1 subunit of the voltage-dependent calcium channel. Neuron, 7(1), 35–44. 10.1016/0896-6273(91)90072-8 [PubMed: 1648940]

Ishida H, Skorobogatov A, Yamniuk AP, & Vogel HJ (2018). Solution structures of the SH3 domains from Shank scaffold proteins and their interactions with Cav1.3 calcium channels. FEBS Lett, 592(16), 2786–2797. 10.1002/1873-3468.13209 [PubMed: 30058071]

Jenkins MA, Christel CJ, Jiao Y, Abiria S, Kim KY, Usachev YM, … Lee A (2010). Ca2+-dependent facilitation of Cav1.3 Ca2+ channels by densin and Ca2+/calmodulin-dependent protein kinase II. J Neurosci, 30(15), 5125–5135. 10.1523/JNEUROSCI.4367-09.2010 [PubMed: 20392935]

Li Q, Lau A, Morris TJ, Guo L, Fordyce CB, & Stanley EF (2004). A syntaxin 1, Galpha(o), and N-type calcium channel complex at a presynaptic nerve terminal: analysis by quantitative immunocolocalization. J Neurosci, 24(16), 4070–4081. 10.1523/JNEUROSCI.0346-04.2004 [PubMed: 15102922]

Lutz AK, Bauer HF, Ioannidis V, Schön M, & Boeckers TM (2022). SHANK3 Antibody Validation: Differential Performance in Western Blotting, Immunocyto- and Immunohistochemistry. Front Synaptic Neurosci, 14, 890231. 10.3389/fnsyn.2022.890231 [PubMed: 35734418]

Marom M, Hagalili Y, Sebag A, Tzvier L, & Atlas D (2010). Conformational changes induced in voltage-gated calcium channel Cav1.2 by BayK 8644 or FPL64176 modify the kinetics

of secretion independently of Ca2+ influx. J Biol Chem, 285(10), 6996–7005. 10.1074/jbc.M109.059865 [PubMed: 20054004]

Martínez-Rivera A, Hao J, Tropea TF, Giordano TP, Kosovsky M, Rice RC, … Rajadhyaksha AM (2017). Enhancing VTA $Ca_V1.3$ L-type Ca^{2+} channel activity promotes cocaine and mood-related behaviors via overlapping AMPA receptor mechanisms in the nucleus accumbens. Mol Psychiatry, 22(12), 1735–1745. 10.1038/mp.2017.9 [PubMed: 28194001]

McNeill RB, & Colbran RJ (1995). Interaction of autophosphorylated Ca2+/calmodulin-dependent protein kinase II with neuronal cytoskeletal proteins. Characterization of binding to a 190-kDa postsynaptic density protein. J Biol Chem, 270(17), 10043–10049. 10.1074/jbc.270.17.10043 [PubMed: 7730306]

Monteiro P, & Feng G (2017). SHANK proteins: roles at the synapse and in autism spectrum disorder. Nat Rev Neurosci, 18(3), 147–157. 10.1038/nrn.2016.183 [PubMed: 28179641]

Moreno CM, Dixon RE, Tajada S, Yuan C, Opitz-Araya X, Binder MD, & Santana LF (2016). Ca(2+) entry into neurons is facilitated by cooperative gating of clustered CaV1.3 channels. Elife, 5. 10.7554/eLife.15744

Naisbitt S, Kim E, Tu JC, Xiao B, Sala C, Valtschanoff J, … Sheng M (1999). Shank, a novel family of postsynaptic density proteins that binds to the NMDA receptor/PSD-95/GKAP complex and cortactin. Neuron, 23(3), 569–582. 10.1016/s0896-6273(00)80809-0 [PubMed: 10433268]

Nakamura Y, Reva M, & DiGregorio DA (2018). Variations in Ca^{2+} influx can alter chelator-based estimates of Ca^{2+} channle-synaptic vesicle coupling distance. J Neurosci, 38(16), 3971–3987. 10.1523/JNEUROSCI.2061-17.2018 [PubMed: 29563180]

Navedo MF, & Santana LF (2013). CaV1.2 sparklets in heart and vascular smooth muscle. J Mol Cell Cardiol, 58, 67–76. 10.1016/j.yjmcc.2012.11.018 [PubMed: 23220157]

Obermair GJ, Schlick B, Di Biase V, Subramanyam P, Gebhart M, Baumgartner S, & Flucher BE (2010). Reciprocal interactions regulate targeting of calcium channel beta subunits and membrane expression of alpha1 subunits in cultured hippocampal neurons. J Biol Chem, 285(8), 5776–5791. 10.1074/jbc.M109.044271 [PubMed: 19996312]

Obermair GJ, Szabo Z, Bourinet E, & Flucher BE (2004). Differential targeting of the L-type Ca2+ channel alpha 1C (CaV1.2) to synaptic and extrasynaptic compartments in hippocampal neurons. Eur J Neurosci, 19(8), 2109–2122. 10.1111/j.0953-816X.2004.03272.x [PubMed: 15090038]

Perfitt TL, Wang X, Dickerson MT, Stephenson JR, Nakagawa T, Jacobson DA, & Colbran RJ (2020). Neuronal L-Type Calcium Channel Signaling to the Nucleus Requires a Novel CaMKIIα-Shank3 Interaction. J Neurosci, 40(10), 2000–2014. 10.1523/JNEUROSCI.0893-19.2020 [PubMed: 32019829]

Peça J, Feliciano C, Ting JT, Wang W, Wells MF, Venkatraman TN, … Feng G (2011). Shank3 mutant mice display autistic-like behaviours and striatal dysfunction. Nature, 472(7344), 437–442. 10.1038/nature09965 [PubMed: 21423165]

Pinggera A, Lieb A, Benedetti B, Lampert M, Monteleone S, Liedl KR, … Striessnig J (2015). CACNA1D de novo mutations in autism spectrum disorders activate Cav1.3 L-type calcium channels. Biol Psychiatry, 77(9), 816–822. 10.1016/j.biopsych.2014.11.020 [PubMed: 25620733]

Ponna SK, Myllykoski M, Boeckers TM, & Kursula P (2017). Structure of an unconventional SH3 domain from the postsynaptic density protein Shank3 at ultrahigh resolution. Biochem Biophys Res Commun, 490(3), 806–812. 10.1016/j.bbrc.2017.06.121 [PubMed: 28647360]

Pym E, Sasidharan N, Thompson-Peer KL, Simon DJ, Anselmo A, Sadreyev R, … Kaplan JM (2017). Shank is a dose-dependent regulator of CaV1 calcium current and CREB target expression. Elife, 6. 10.7554/eLife.18931

Shanks NF, Maruo T, Farina AN, Ellisman MH, & Nakagawa T (2010). Contribution of the global subunit structure and stargazin on the maturation of AMPA receptors. J Neurosci, 30(7), 2728–2740. 10.1523/JNEUROSCI.5146-09.2010 [PubMed: 20164357]

Sheng M, & Hoogenraad CC (2007). The postsynaptic architecture of excitatory synapses: a more quantitative view. Annu Rev Biochem, 76, 823–847. 10.1146/annurev.biochem.76.060805.160029 [PubMed: 17243894]

Sheng M, & Kim E (2000). The Shank family of scaffold proteins. J Cell Sci, 113 (Pt 11), 1851–1856. 10.1242/jcs.113.11.1851 [PubMed: 10806096]

Simms BA, & Zamponi GW (2014). Neuronal voltage-gated calcium channels: structure, function, and dysfunction. Neuron, 82(1), 24–45. 10.1016/j.neuron.2014.03.016 [PubMed: 24698266]

Singh A, Gebhart M, Fritsch R, Sinnegger-Brauns MJ, Poggiani C, Hoda JC, … Koschak A (2008). Modulation of voltage- and Ca2+-dependent gating of CaV1.3 L-type calcium channels by alternative splicing of a C-terminal regulatory domain. J Biol Chem, 283(30), 20733–20744. 10.1074/jbc.M802254200 [PubMed: 18482979]

Stanika R, Campiglio M, Pinggera A, Lee A, Striessnig J, Flucher BE, & Obermair GJ (2016). Splice variants of the $Ca_V1.3$ L-type calcium channel regulate dendritic spine morphology. Sci Rep, 6, 34528. 10.1038/srep34528 [PubMed: 27708393]

Stern MD (1992). Buffering of calcium in the vicinity of a channel pore. Cell Calcium, 13(3), 183–192. 10.1016/0143-4160(92)90046-u [PubMed: 1315621]

Striessnig J, & Koschak A (2008). Exploring the function and pharmacotherapeutic potential of voltage-gated Ca2+ channels with gene knockout models. Channels (Austin), 2(4), 233–251. 10.4161/chan.2.4.5847 [PubMed: 18719397]

Tadross MR, Tsien RW, & Yue DT (2013). Ca2+ channel nanodomains boost local Ca2+ amplitude. Proc Natl Acad Sci U S A, 110(39), 15794–15799. 10.1073/pnas.1313898110 [PubMed: 24019485]

Tan BZ, Jiang F, Tan MY, Yu D, Huang H, Shen Y, & Soong TW (2011). Functional characterization of alternative splicing in the C terminus of L-type CaV1.3 channels. J Biol Chem, 286(49), 42725–42735. 10.1074/jbc.M111.265207 [PubMed: 21998309]

Tian Y, Corkey RF, Yaney GC, Goforth PB, Satin LS, & Moitoso de Vargas L (2008). Differential modulation of L-type calcium channel subunits by oleate. Am J Physiol Endocrinol Metab, 294(6), E1178–1186. 10.1152/ajpendo.90237.2008 [PubMed: 18430963]

Verpelli C, Dvoretskova E, Vicidomini C, Rossi F, Chiappalone M, Schoen M, … Sala C (2011). Importance of Shank3 protein in regulating metabotropic glutamate receptor 5 (mGluR5) expression and signaling at synapses. J Biol Chem, 286(40), 34839–34850. 10.1074/jbc.M111.258384 [PubMed: 21795692]

Vierra NC, Kirmiz M, van der List D, Santana LF, & Trimmer JS (2019). Kv2.1 mediates spatial and functional coupling of L-type calcium channels and ryanodine receptors in mammalian neurons. Elife, 8. 10.7554/eLife.49953

Wang S, Stanika RI, Wang X, Hagen J, Kennedy MB, Obermair GJ, … Lee A (2017). Densin-180 Controls the Trafficking and Signaling of L-Type Voltage-Gated Ca. J Neurosci, 37(18), 4679–4691. 10.1523/JNEUROSCI.2583-16.2017 [PubMed: 28363979]

Wang X, Marks CR, Perfitt TL, Nakagawa T, Lee A, Jacobson DA, & Colbran RJ (2017). A novel mechanism for Ca^{2+}/calmodulin-dependent protein kinase II targeting to L-type Ca^{2+} channels that initiates longrange signaling to the nucleus. J Biol Chem, 292(42), 17324–17336. 10.1074/jbc.M117.788331 [PubMed: 28916724]

Weick JP, Groth RD, Isaksen AL, & Mermelstein PG (2003). Interactions with PDZ proteins are required for L-type calcium channels to activate cAMP response element-binding protein-dependent gene expression. J Neurosci, 23(8), 3446–3456. [PubMed: 12716953]

Wheeler DG, Groth RD, Ma H, Barrett CF, Owen SF, Safa P, & Tsien RW (2012). Ca(V)1 and Ca(V)2 channels engage distinct modes of Ca(2+) signaling to control CREB-dependent gene expression. Cell, 149(5), 1112–1124. 10.1016/j.cell.2012.03.041 [PubMed: 22632974]

Wu CH, Tatavarty V, Jean Beltran PM, Guerrero AA, Keshishian H, Krug K, … Turrigiano GG (2022). A bidirectional switch in the Shank3 phosphorylation state biases synapses toward up- or downscaling. Elife, 11. 10.7554/eLife.74277

Wu X, & Hammer JA (2021). ZEISS Airyscan: Optimizing Usage for Fast, Gentle, Super-Resolution Imaging. Methods Mol Biol, 2304, 111–130. 10.1007/978-1-0716-1402-0_5 [PubMed: 34028713]

Zhang H, Fu Y, Altier C, Platzer J, Surmeier DJ, & Bezprozvanny I (2006). Ca1.2 and CaV1.3 neuronal L-type calcium channels: differential targeting and signaling to pCREB. Eur J Neurosci, 23(9), 2297–2310. 10.1111/j.1460-9568.2006.04734.x [PubMed: 16706838]

Zhang H, Maximov A, Fu Y, Xu F, Tang TS, Tkatch T, … Bezprozvanny I (2005). Association of CaV1.3 L-type calcium channels with Shank. J Neurosci, 25(5), 1037–1049. 10.1523/JNEUROSCI.4554-04.2005 [PubMed: 15689539]

Zhang J, Carver CM, Choveau FS, & Shapiro MS (2016). Clustering and Functional Coupling of Diverse Ion Channels and Signaling Proteins Revealed by Super-resolution STORM Microscopy in Neurons. Neuron, 92(2), 461–478. 10.1016/j.neuron.2016.09.014 [PubMed: 27693258]

Zhou Y, Kaiser T, Monteiro P, Zhang X, Van der Goes MS, Wang D, … Feng G (2016). Mice with Shank3 Mutations Associated with ASD and Schizophrenia Display Both Shared and Distinct Defects. Neuron, 89(1), 147–162. 10.1016/j.neuron.2015.11.023 [PubMed: 26687841]

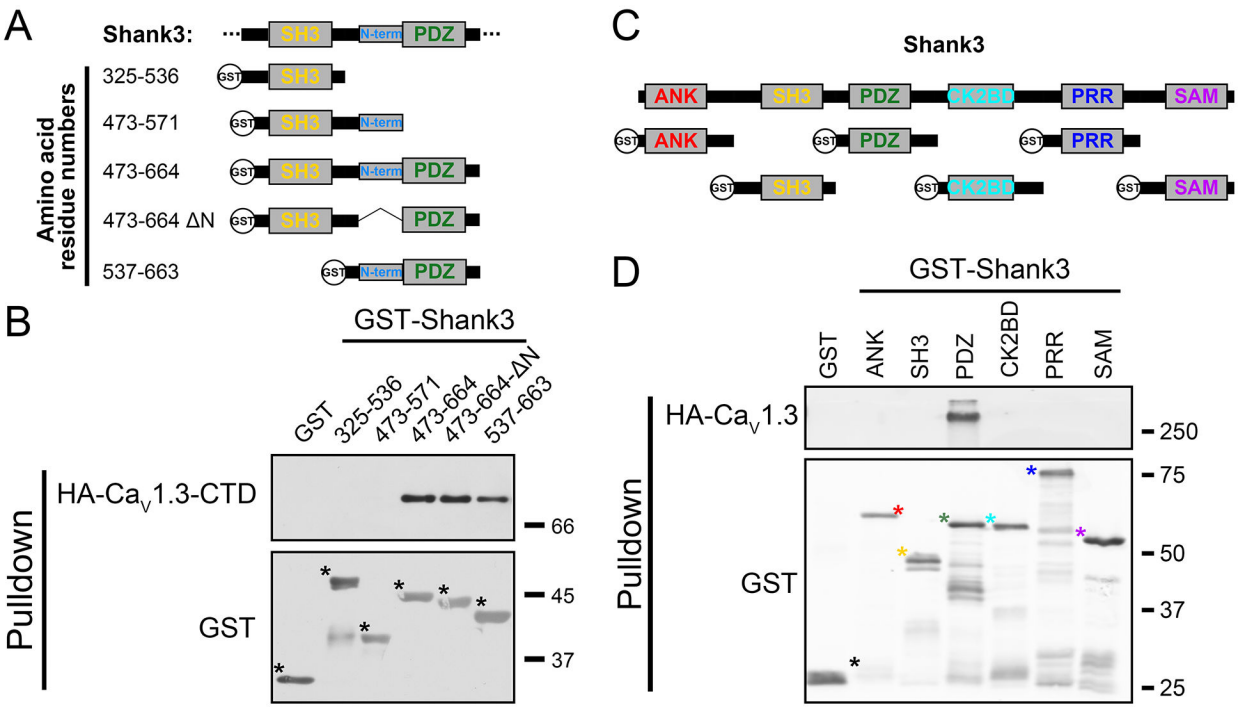

Figure 1. The Shank3 PDZ domain is necessary and sufficient for interaction with the $Ca_V1.3_L$ C-terminal domain.

A) Schematic of Shank3 truncations and deletions expressed as Glutathione-S-transferase (GST) fusion proteins for use in panel B, with amino acid residue numbers. The ΔN deletion removed residues 543-564. B) An anti-HA immunoblot (top) of glutathione agarose co-sedimentation assays revealed that HA-$Ca_V1.3_L$-CTD binds to all GST-Shank3 proteins containing the PDZ domain but not to proteins lacking the PSD95/DlgA/Zo-1 domain (PDZ) domain. Full-length GST fusion proteins are marked with asterisks on the corresponding GST immunoblot (bottom). C) Domain structure of full-length Shank3 and six GST-Shank3 fusion proteins spanning the entire Shank3 protein used in panel D. Canonical Shank3 domains are depicted as gray boxes: ANK = ankyrin-rich repeats, aa 1-324; SH3 = Src homology 3 domain, aa 325-536; PDZ = PSD95/Dlg1/zo-1 domain, aa 537-828; CK2BD = CaMKII binding domain, aa 829-1130; PRR = proline-rich region, aa 1131-1467; SAM = Sterile alpha motif, aa 1468-1740. D) An anti-HA immunoblot (top) of a glutathione agarose co-sedimentation assay detected binding of full-length HA-$Ca_V1.3_L$ α subunit only to the GST-Shank3-PDZ domain protein. Full-length GST fusion proteins are marked with color coded asterisks on the corresponding GST immunoblot (bottom). Panels B and D are representative of three independent biological replicates.

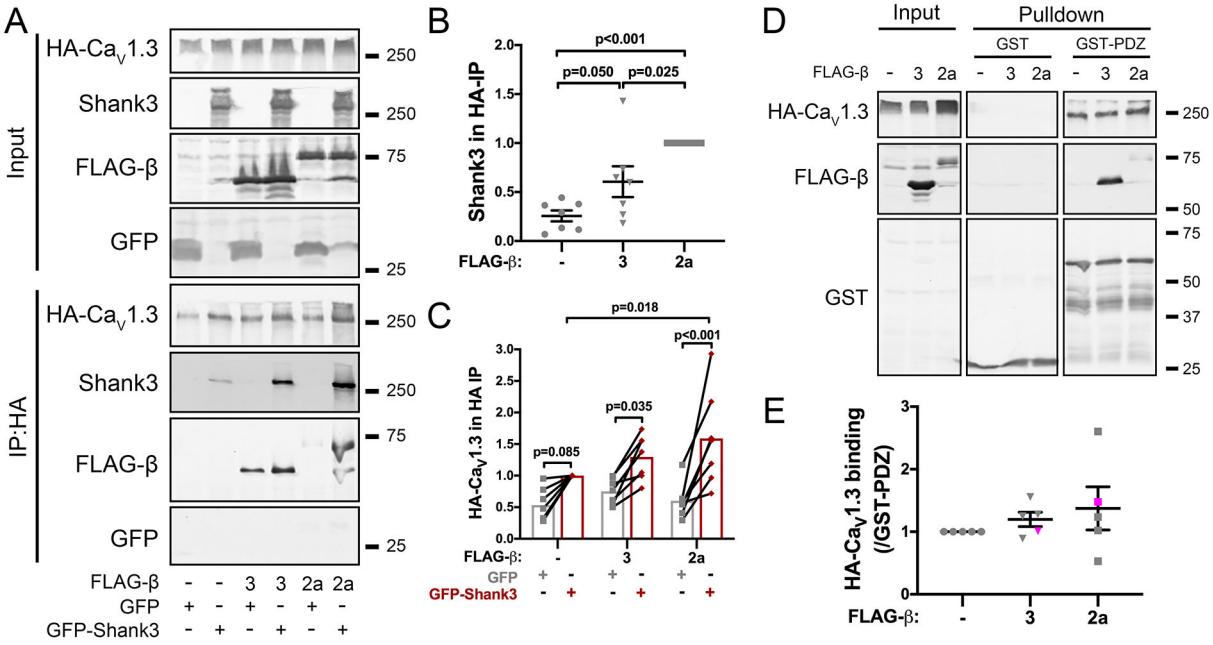

Figure 2. Association of GFP-Shank3 with HA-$Ca_V1.3_L$ is facilitated by co-expression of FLAG-β subunits.

A) Representative immunoblots of HA, Shank3, FLAG, and enhanced green fluorescent protein (GFP) signals in the input (top) and anti-HA immune complexes (bottom) isolated from soluble fractions of HEK293T cells co-expressing HA-$Ca_V1.3_L$ with GFP or GFP-Shank3, with or without FLAG-β2a or -β3 subunits, as indicated below. Quantifications of the Shank3 (B) and HA-$Ca_V1.3_L$ (C) signals in HA-IPs: mean ± SEM, n = 7 independent transfections. B: One-way ANOVA followed by Tukey's post hoc test. C: Two-way ANOVA followed by Sidak's post hoc test when comparing GFP to GFP-Shank3 or by Turkey's post hoc test when comparing between no β, β3, and β2a. D) Representative immunoblots of HA, FLAG, and GST signals in soluble fractions of HEK293T cells co-expressing HA-$Ca_V1.3_L$, α2δ, with or without Flag-β2a or -β3 subunits (input) and in glutathione agarose co-sedimentation assays following incubation with the GST-Shank3-PDZ domain (2 μg). E) Quantification of HA-$Ca_V1.3_L$ signals in GST complexes obtained from 5 independent transfected cell samples incubated with two different GST-Shank3-PDZ domain constructs containing either residues 537-828 (as in Fig. 1D: 1 replicate, magenta symbols) or residues 572-691 (4 replicates, gray symbols). Mean ± SEM, n = 5. No significant differences between groups by one-way ANOVA.

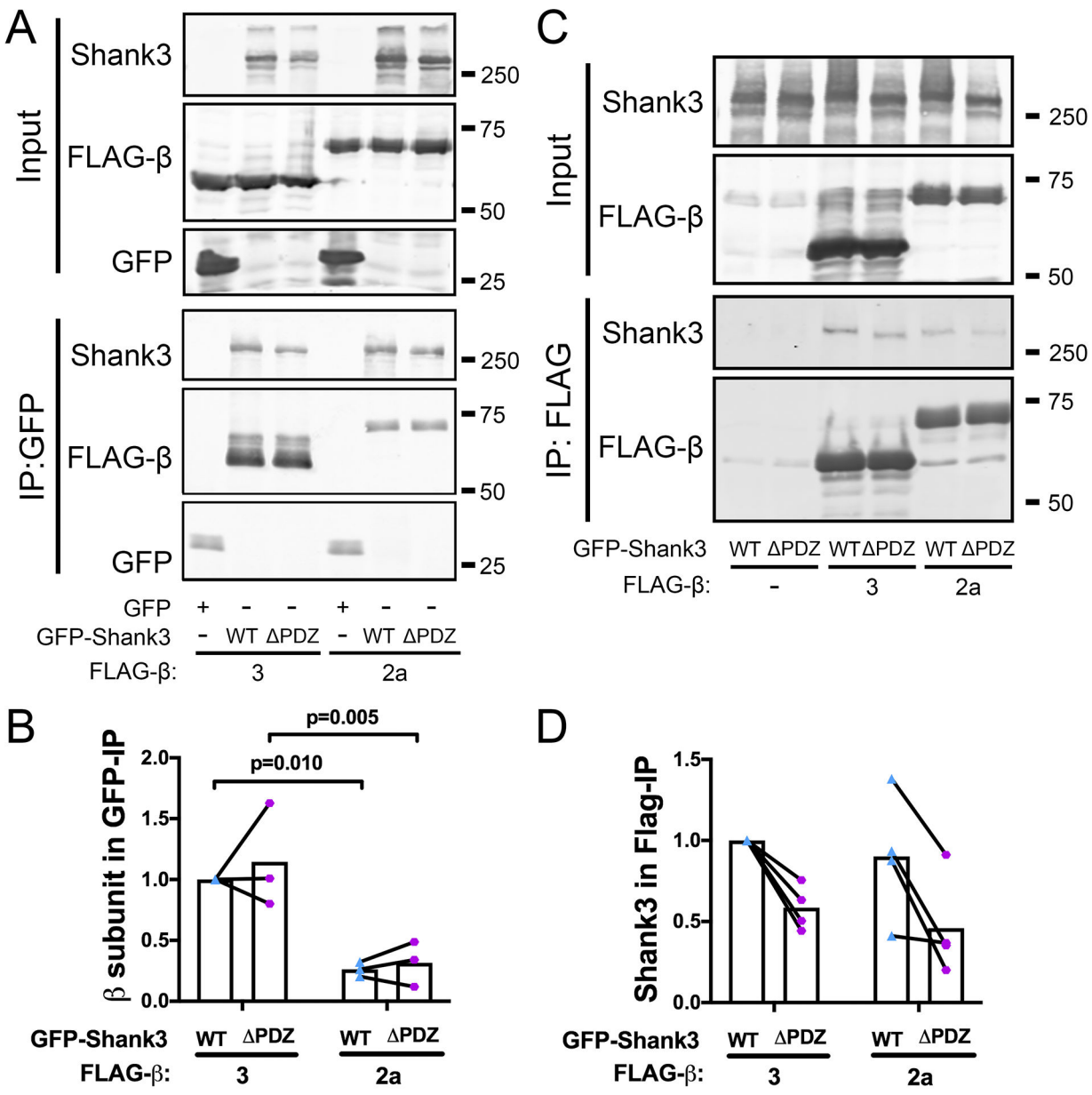

Figure 3. Association of FLAG-β subunits with GFP-Shank3.

A) Representative Shank3, FLAG and GFP immunoblots of soluble fractions (Input) of HEK293T cells co-expressing GFP (control) or GFP-Shank3 (WT or ΔPDZ) with or without FLAG-β3 or -β2a subunits, and corresponding isolated anti-GFP immune complexes. B) Quantification of FLAG-β subunit signals in GFP-Shank3 immune complexes from 3 independent transfected cell replicates. Mean ± SEM: two-way ANOVA followed by Sidak's post hoc test. C) Representative Shank3 and Flag immunoblots of inputs and anti-FLAG immune complexes isolated from HEK293T cells expressing GFP-Shank3 (WT or ΔPDZ) with or without FLAG-β3 or β2a. D) Quantification of GFP-Shank3 signals in FLAG-β immune complexes from 4 independent transfected cell replicates. Mean ± SEM: two-way ANOVA followed by Sidak's post hoc test.

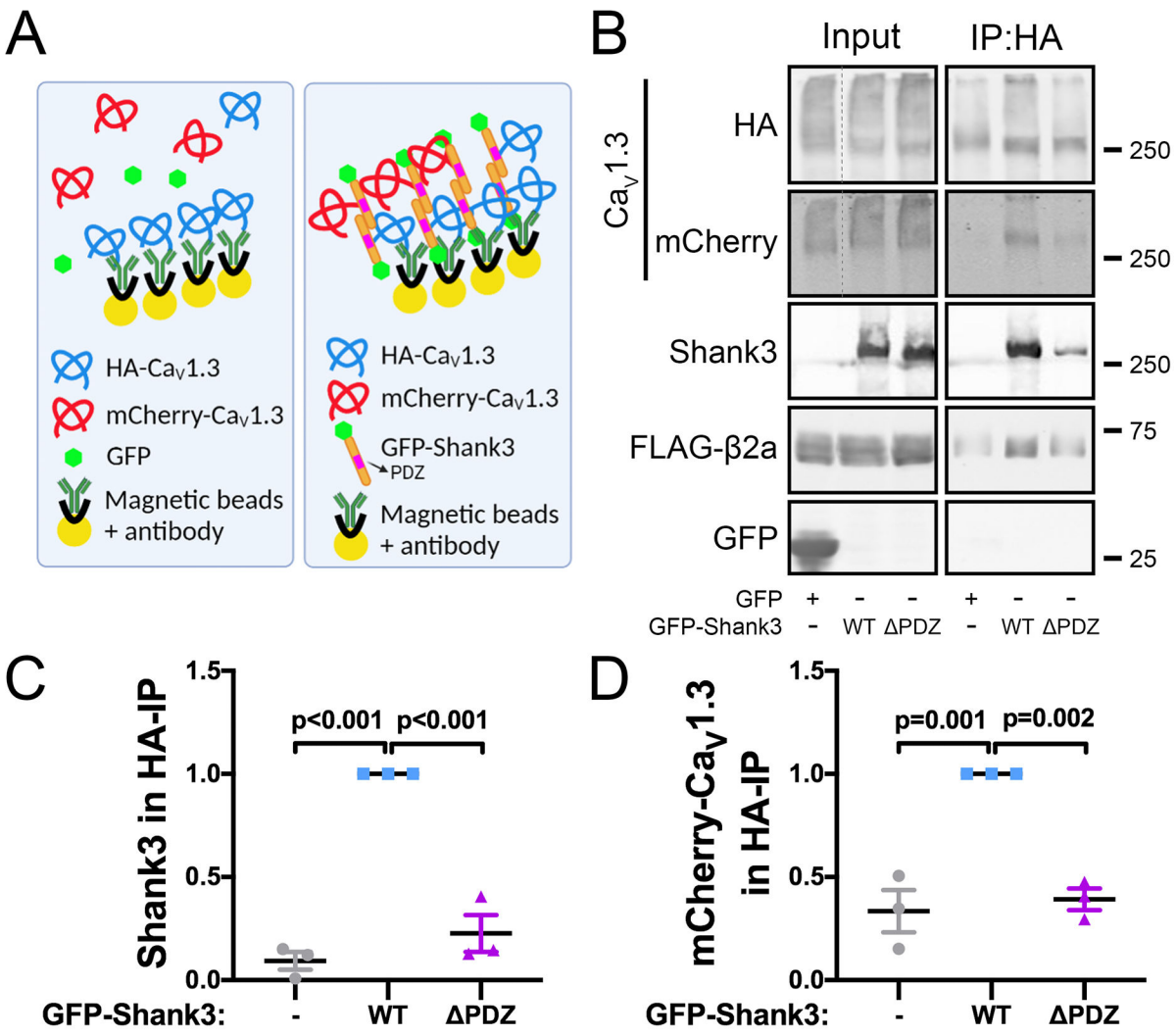

Figure 4. Assembly of multi-Ca$_V$1.3$_L$ complexes require the Shank3 PDZ domain.

A) Schematic of experimental design to test the hypothesis that Shank3 mediates the assembly of complexes containing multiple Ca$_V$1.3$_L$ α1 subunits. In the presence of GFP (left), mCherry-Ca$_V$1.3$_L$ cannot associate with anti-HA IPs. PDZ domains in GFP-Shank3 dimers associate with both HA- and mCherry-Ca$_V$1.3$_L$, mediating the isolation of both GFP-Shank3 and mCherry-Ca$_V$1.3$_L$ by anti-HA IP (right). B) Representative immunoblots for HA- and mCherry-Ca$_V$1.3$_L$, FLAG-β2a, Shank3 and GFP in the inputs and anti-HA immunoprecipitations (IPs) from soluble fractions of HEK293T cells co-expressing HA- and mCherry-tagged Ca$_V$1.3$_L$ and FLAG-β2a with either GFP or GFP-Shank3 (WT or ΔPDZ). Dashed lines in HA and mCherry input blots indicated that an intervening lane loaded with molecular weight markers was excised from the image (see the original blot in Supplemental Figure 11). C) Quantification of GFP/GFP-Shank3 (WT or ΔPDZ) signals in HA-IPs, normalized to HA-Ca$_V$1.3$_L$ signal, from three independent transfections. D) Quantification of mCherry-Ca$_V$1.3$_L$ signals in HA-IPs, normalized to HA-Ca$_V$1.3$_L$ signal, from three independent transfections. Mean ± SEM: One-way ANOVA followed by Tukey's post hoc test.

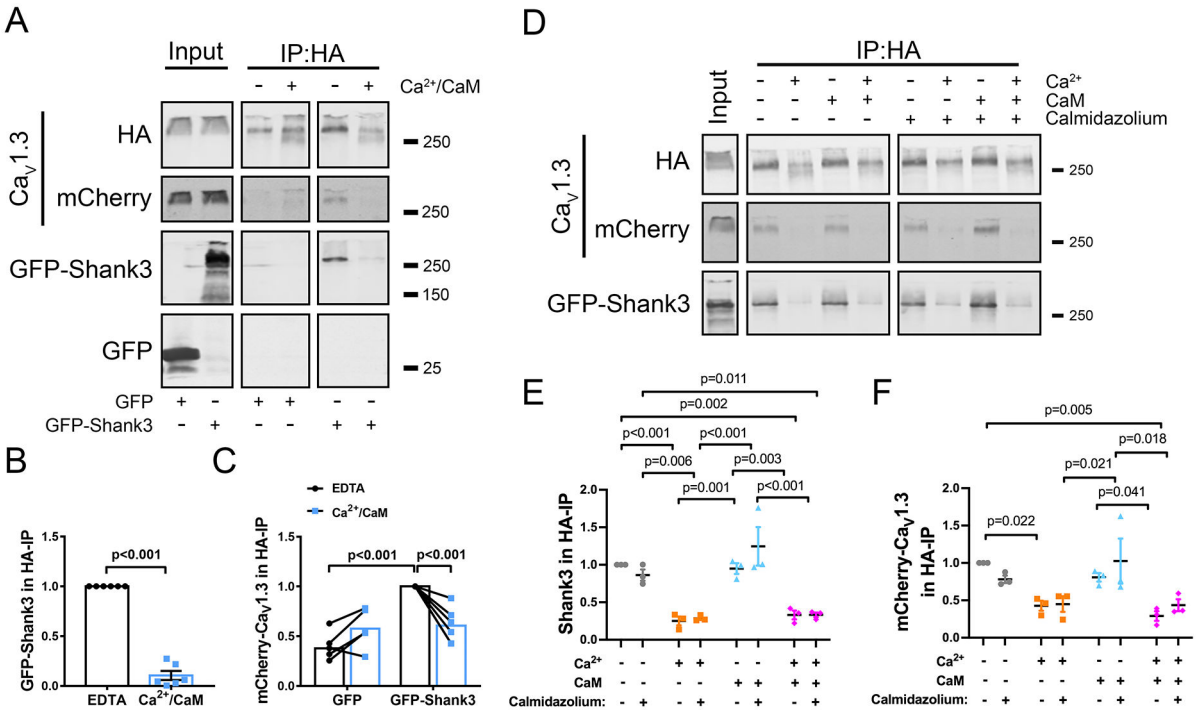

Figure 5. Assembly of multi-$Ca_V1.3_L$ complexes by Shank3 is suppressed by Ca^{2+}.

A) Representative immunoblots for HA- and mCherry-$Ca_V1.3_L$, and GFP in inputs and anti-HA immunoprecipitations (IPs) from soluble fractions of HEK293T cells co-expressing HA- and mCherry-tagged $Ca_V1.3_L$ and FLAG-β2a with either GFP or GFP-Shank3 without (EDTA) or with Ca^{2+}/CaM addition. B) Quantification of GFP-Shank3 in HA-IPs from six independent transfections; GFP-Shank3 signals were first normalized to the HA-signal in the corresponding IP, and then to the EDTA control; analyzed using a one-sample t-test. C) Quantification of mCherry-$Ca_V1.3_L$ in HA-IPs from six independent transfections; mCherry-$Ca_V1.3_L$ signals were first normalized to the HA-signal in the corresponding IP, and then to the EDTA/GFP-Shank3 control; analyzed using a two-way ANOVA followed by Sidak's post hoc test. D) Representative immunoblots for HA- and mCherry-$Ca_V1.3_L$, and GFP-Shank3 in inputs and anti-HA immunoprecipitations (IPs) from soluble fractions of HEK293T cells co-expressing HA- and mCherry-tagged $Ca_V1.3_L$ and FLAG-β3 with GFP-Shank3 with no additions and following addition of Ca^{2+} alone, CaM alone, or Ca^{2+}/CaM, in the absence or presence of calmidazolium (50 μM). Quantification of E) GFP-Shank3 and F) mCherry-$Ca_V1.3_L$ in HA-IPs from three independent transfections; signals were first normalized to the HA-signal in the corresponding IP, and then to the "no addition" condition; Two-way ANOVA followed by Sidak's post hoc test when comparing without and with calmidazolium or by Tukey's post hoc test when comparing between four conditions.

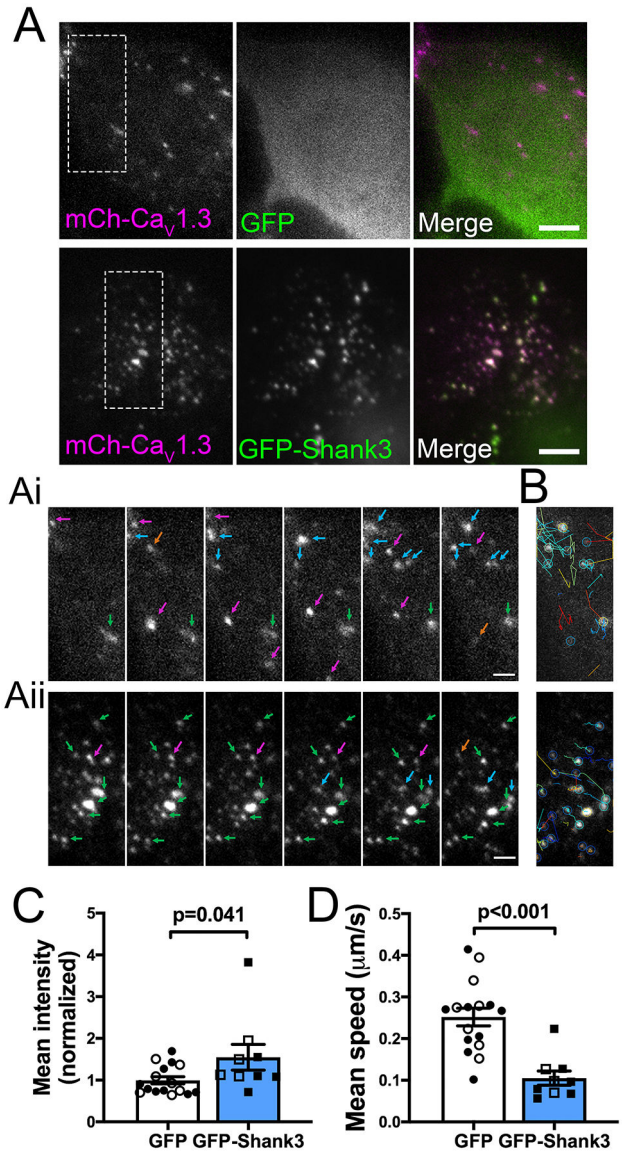

Figure 6. GFP-Shank3 modulates mCherry-$Ca_V1.3_L$ dynamics in HEK293 cell plasma membranes.

A) Representative single channel and merged TIRF microscope images of live HEK293 cells co-expressing mCherry-$Ca_V1.3_L$, FLAG-β3 and either GFP (top) or GFP-Shank3 (bottom). Enlarged time lapse mCherry images (0, 30, 60, 90, 120 and 150 s) within the indicated rectangular regions of interest are shown in Ai and Aii (Supplemental Movies 1 and 2 show the entire time course). Colored arrows indicate the properties of selected mCherry puncta: Green, puncta present throughout; Red, puncta that disappear; Orange, puncta that appear transiently; Blue, puncta that appear but remain to the last time point. Scale bars, 5 μm in A and 2 μm in Ai and Aii. B) Tracking lateral movement of individual $Ca_V1.3_L$ puncta in the plane of the TIRF image using the FIJI TrackMate plug-in, superimposed on images from the last time point in Ai and Aii. C) Quantification of the average intensity of mCherry-$Ca_V1.3_L$ puncta. D) Quantification of the speed of lateral movement of mCherry-$Ca_V1.3_L$ puncta (TrackMate). Data in panels C and D were collected from 16 (GFP) or

9 (GFP-Shank3) cells from 5 independent transfections. Open and solid symbols are from cells transfected with FLAG-β2a or FLAG-β3, respectively. Mean ± SEM: unpaired t-test.

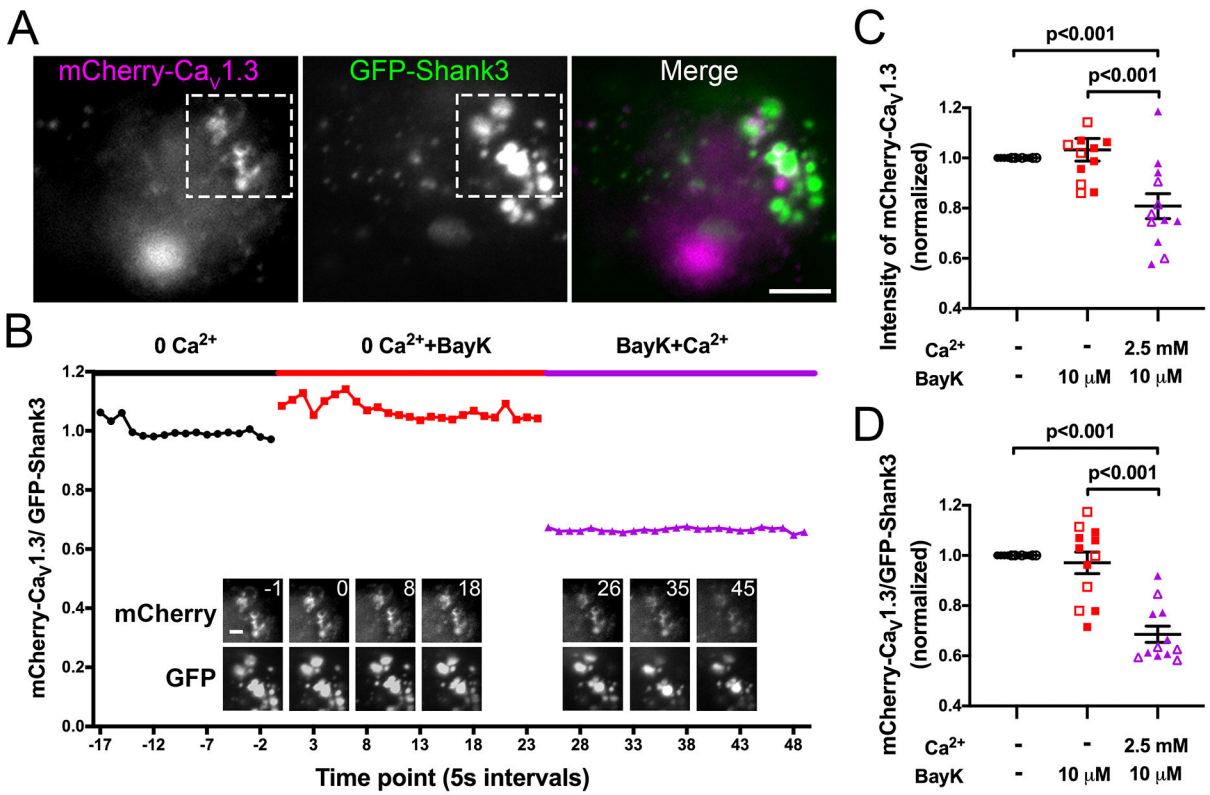

Figure 7. Ca^{2+} influx dissociates GFP-Shank3 from mCherry-$Ca_V1.3_L$ in live HEK293 cells.

A) Representative mCherry, GFP and merged TIRF microscope image of a live HEK293 cell co-expressing mCherry-$Ca_V1.3_L$, FLAG-β3 and GFP-Shank3 at the start of the experiment (scale bar, 5 μm). B) The cell was imaged every 5 s for 2-3 minutes each in "no Ca^{2+}" buffer, following the addition of BayK 8644 (10 μM), and following the further addition of Ca^{2+} (2.5 mM $CaCl_2$). No images were collected for ~1 min during each buffer addition. The ratio of mCherry-$Ca_V1.3_L$ to GFP-Shank3 signal intensity in the region of interest (highlighted in panel A) was quantified at each time point. Insets show enlarged ROI images of mCherry-$Ca_V1.3_L$ (top row) and GFP-Shank3 (bottom row) images at selected time points (scale bar, 2 μm). Supplemental Movie 3 shows all time points. C) Summary of average mCherry-$Ca_V1.3_L$ signal intensity from all time points under each condition, normalized to the "no Ca^{2+}" condition. D) Ratio of mCherry-$Ca_V1.3_L$ to GFP-Shank3 signal intensity from all time points under each condition, normalized to the "no Ca^{2+}" condition. Data in panels C and D were collected from 12 cells analyzed from six transfections (open and solid symbols indicate expressing FLAG-β2a or FLAG-β3, respectively). One-way ANOVA followed by Tukey's post hoc test was used for comparisons.

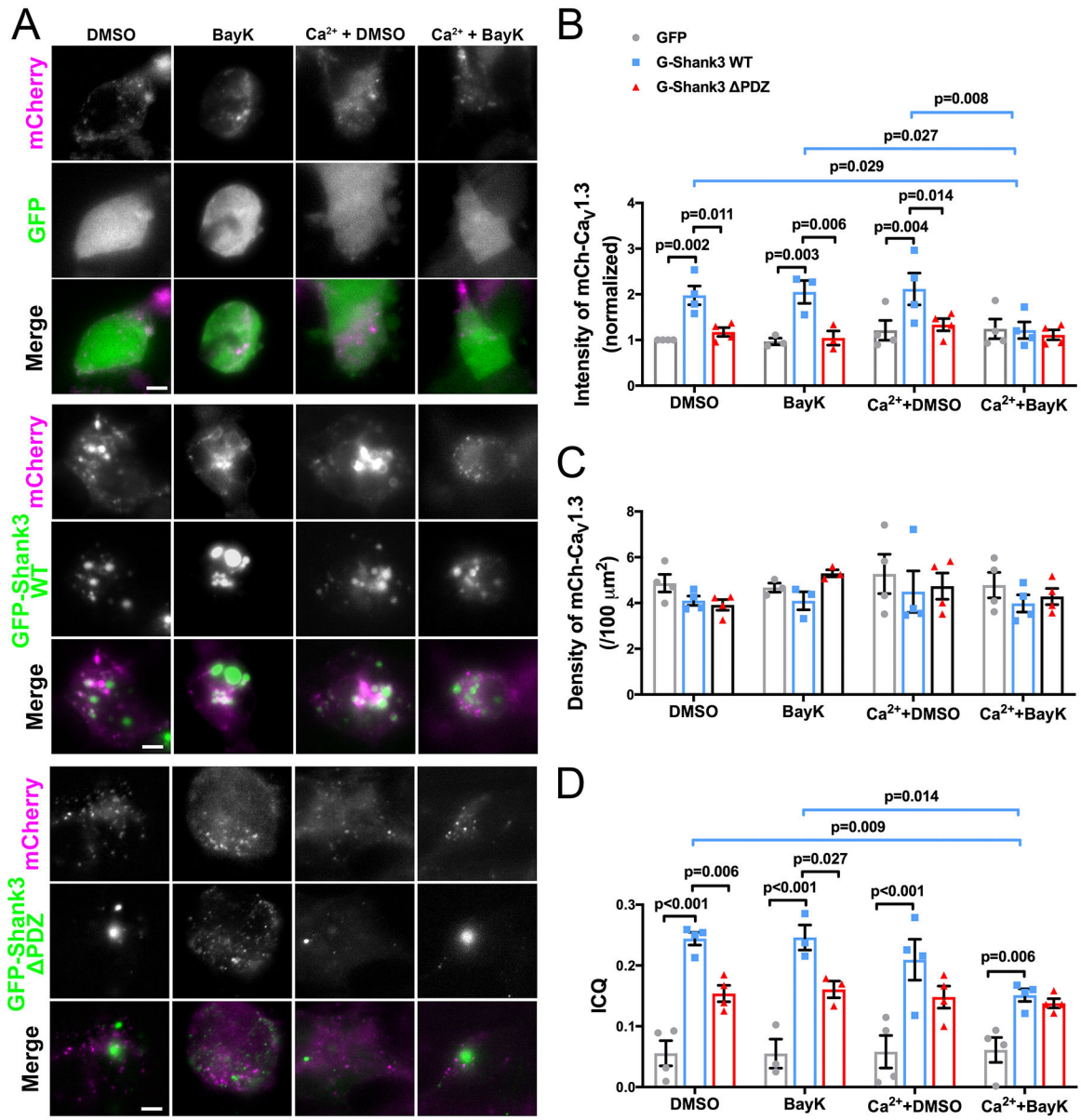

Figure 8. Shank3 and Ca^{2+} influx regulate mCherry-$Ca_V1.3_L$ puncta intensity in HEK293 cell plasma membranes.

A) Representative TIRF microscope images of single HEK293 cells co-expressing mCherry-$Ca_V1.3_L$ and FLAG-β3 with either GFP or GFP-Shank3 (WT or ΔPDZ), fixed following incubation for 10-15 min in "no Ca^{2+}" or Ca^{2+} buffer with vehicle (DMSO) or BayK 8644 (BayK, 10 μM), as indicated (scale bar, 5 μm). B) Quantification of mCherry-$Ca_V1.3_L$ puncta intensity. C) Quantification of mCherry-$Ca_V1.3_L$ puncta density. D) Intensity correlation analysis of GFP/mCherry colocalization. Panels B-D plot the mean ± SEM, with each data point representing the average of 7-15 cells per condition from 3 or 4 independent transfections. Data were compared using a two-way ANOVA followed by Tukey's multiple comparisons test.

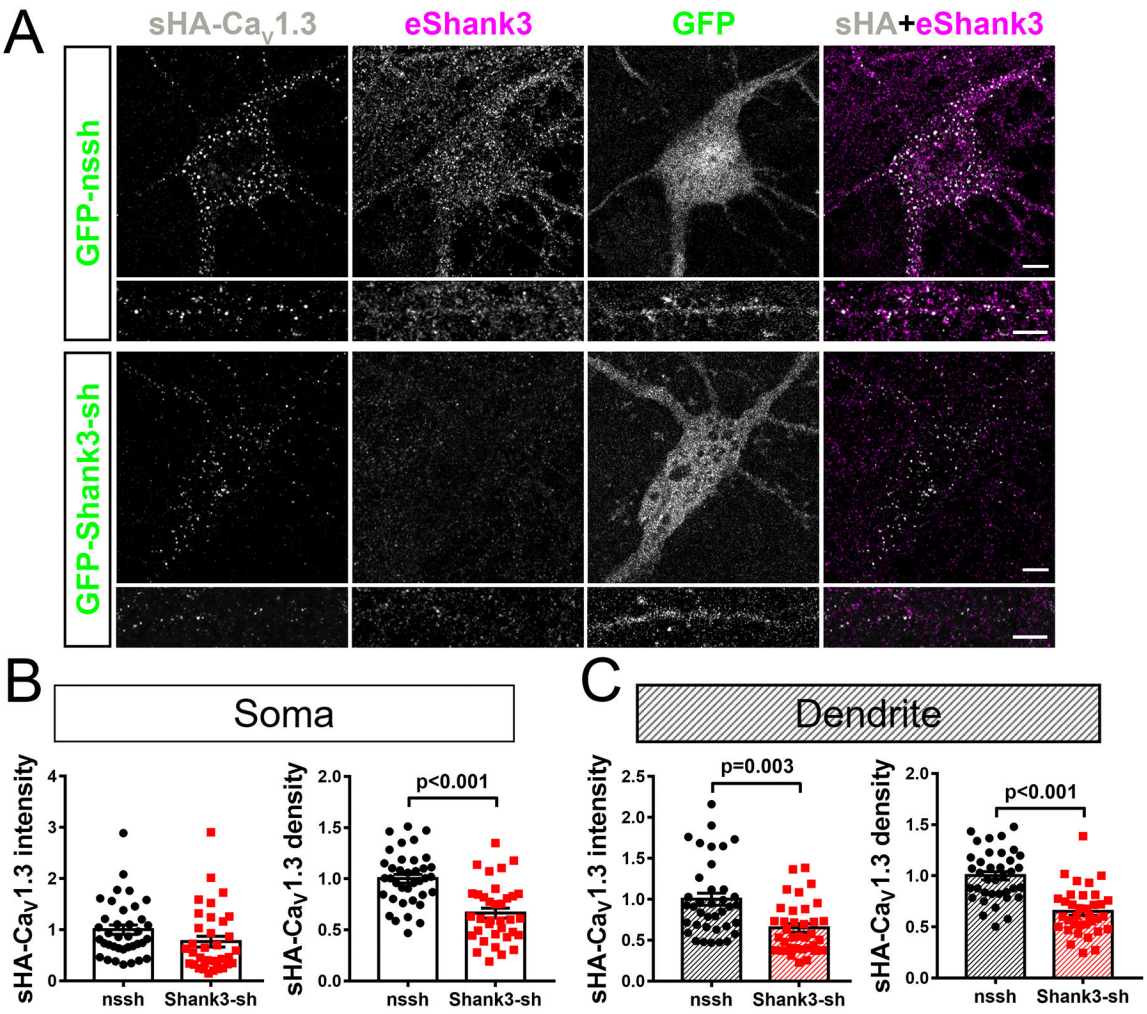

Figure 9. Effects of Shank3 knock-down on surface-expressed $Ca_V1.3_L$ puncta in neurons.

Primary rat hippocampal neurons expressing sHA-$Ca_V1.3_L$ and FLAG-β3 with either GFP-nonsense shRNA (GFP-nssh) or GFP-Shank3 shRNA (GFP-Shank3-sh) were live-immunostained for the HA tag at DIV21, fixed, permeabilized and then immunostained for endogenous Shank3 (eShank3). Neurons were imaged using Airyscan super-resolution confocal microscopy. A) Representative images of soma and dendrites. Scale bar, 5 μm. B) and C) Quantification of sHA-$Ca_V1.3_L$ cluster intensity and cluster density, respectively, of n = 37 (GFP-nssh) or 35 (GFP-Shank3-sh) neurons from three independent cultures/transfections; comparisons made using an unpaired t-test. Within each biological replicate, the sHA-$Ca_V1.3$ intensities and densities in each neuron were normalized to the mean of the corresponding values in the nssh control neurons.

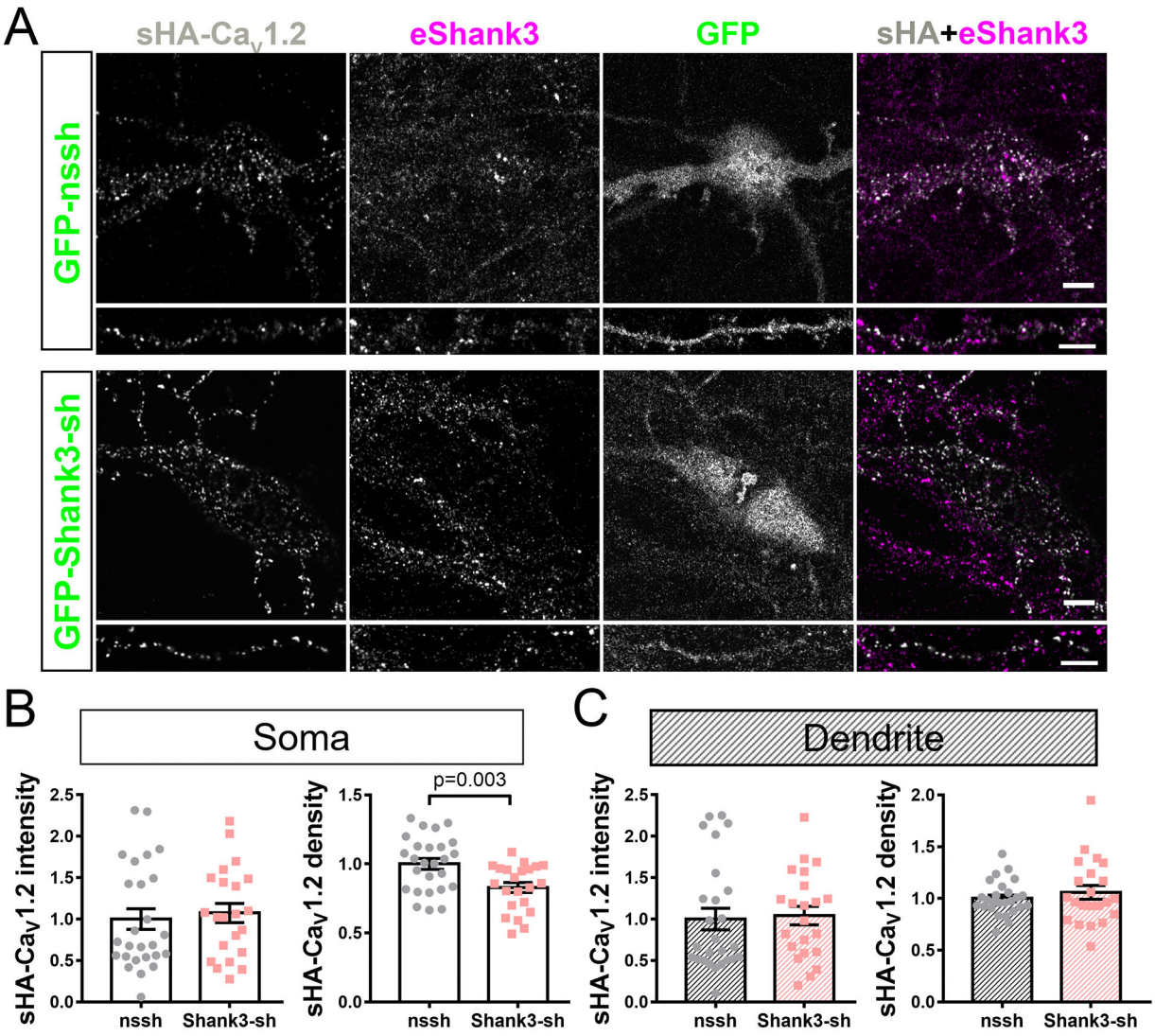

Figure 10. Shank3 knock-down has no effect on $Ca_V1.2$ surface puncta intensity in neurons.

Primary rat hippocampal neuron (14 DIV) expressing sHA-$Ca_V1.2$ and FLAG-β3 with either GFP-nonsense shRNA (GFP-nssh) or GFP-Shank3 shRNA (GFP-Shank3-sh) were live-immunostained for the HA tag at DIV21, fixed, permeabilized and then immunostained for endogenous Shank3 (eShank3). Neurons were imaged using Airyscan super-resolution confocal microscopy. A) Representative images of soma and dendrites. Scale bar, 5 μm. B) and C) Quantification of sHA-$Ca_V1.2$ cluster intensity and cluster density from n = 26 (GFP-nssh) or 22 (GFP-Shank3-sh) neurons from three independent cultures/transfections; comparisons made using an unpaired t-test. Within each biological replicate, the sHA-$Ca_V1.2$ intensities and densities in each neuron were normalized to the mean of the corresponding values in the nssh control neurons.

Key Resources Table

REAGENT or RESOURCE	SOURCE	IDENTIFIER or GENBANK ACCESSION#
Antibodies		
rabbit monoclonal anti-HA (C29F4)	Cell Signaling	Cat# 3724S
mouse monoclonal anti-HA.11	BioLegend	Cat# 901502
mouse monoclonal anti-mCherry (1C51)	Novus Biologicals	Cat# NBP-96752
mouse anti-GFP (clone 1C9A5)	Vanderbilt Antibody and Protein Resource	
rabbit monoclonal anti-Shank3 (D5K6R)	Cell Signaling	Cat# 64555
mouse monoclonal anti-Flag M2	Sigma	Cat# F3165
rabbit anti-Flag M2	Cell Signaling	Cat# 2368
mouse monoclonal anti-CaMKIIα (6G9)	Invitrogen	Cat# MA1-048
p-CaMKIIα (Thr 286)-R	Santa Cruz	Cat# sc-12886-R
mouse monoclonal anti-GST (clone D1 and D5)	Vanderbilt Antibody and Protein Resource	
HRP-conjugated anti-rabbit	Promega	Cat# W4011
HRP-conjugated anti-mouse	Promega	Cat# W4021
IR dye-conjugated donkey anti-mouse 800CW	LI-COR Biosciences	Cat# 926–32212
IR dye-conjugated donkey anti-rabbit 680LT	LI-COR Biosciences	Cat# 926–68023
rabbit monoclonal anti-HA (C29F4)	Cell Signaling	Cat# 3724S
rabbit monoclonal anti-Shank3 (D5K6R)	Cell Signaling	Cat# 64555
donkey anti-mouse Alexa Fluor 647	Thermo Fisher Scientific	Cat# A-31571
donkey anti-rabbit Alexa Fluor 546	Thermo Fisher Scientific	Cat# A-10040
Purified proteins		
calmodulin	homemade	
CaMKIIα	homemade	
DNA constructs		
$Ca_V1.3$ α1	Rattus norvegicus	AF370010
pCGNH (N-terminal HA tag) pmCherry-C1 pCGNO (external HA tag)	(X. Wang et al., 2017) Xiaohan Wang created in the lab (X. Wang et al., 2017) This construct was created according to (Altier et al., 2002)	
Ca_V α2δ	Oryctolagus cuniculus	M21948
pCDNA	(X. Wang et al., 2017)	
Ca_V β3	Rattus norvegicus	M88751
pCMV-Flag	(X. Wang et al., 2017)	
Ca_V β2a	Rattus norvegicus	M80545
pCMV-Flag	(X. Wang et al., 2017)	
Shank3	Rattus norvegicus	a gift from Dr. Craig Garner

REAGENT or RESOURCE	SOURCE	IDENTIFIER or GENBANK ACCESSION#
EGFP-C1	(Perfitt et al., 2020)	
pGEX4T-1	(Perfitt et al., 2020)	
$Ca_V1.2$ α1	Rattus norvegicus	a gift from Dr. Gerald Zamponi
pCGNO (external HA tag) *	Xiaohan Wang created in the lab	
pLL3.7 (construct expressing shRNA)	(Dittgen et al., 2004)	a gift from Dr. Luk Van Parijs
Nonsense shRNA	(Boudkkazi et al., 2014)	5'-TCGCTTGGGCGAGAGTAAG-3'
Shank3 shRNA	(Verpelli et al., 2011)	5'-GGAAGTCACCAGAGGACAAGA-3'
Chemicals		
Bay K8644	TOCRIS	Cat# 1544
DMSO	Sigma	D8418
Calmidazolium chloride	TOCRIS	Cat# 2561
Cell lines		
Human: HEK293T	ATCC	CRL-3216
Human: HEK293	ATCC	CRL-1573

* After these studies were mostly completed, we detected a mutation in the cDNA encoding sHA-$Ca_V1.2$ which results in a Lys^{2055} mutation to Asn, 86 amino acids away from the C-terminus.